

A nonconforming Trefftz virtual element method for the Helmholtz problem: numerical aspects

Lorenzo Mascotto*, Ilaria Perugia*, Alexander Pichler*

Abstract

We discuss the implementation details and the numerical performance of the recently introduced nonconforming Trefftz virtual element method [37] for the 2D Helmholtz problem. In particular, we present a strategy to significantly reduce the ill-conditioning of the original method; such a recipe is based on an automatic filtering of the basis functions edge by edge, and therefore allows for a notable reduction of the number of degrees of freedom. A widespread set of numerical experiments, including an application to acoustic scattering, the h -, p -, and hp -versions of the method, is presented. Moreover, a comparison with other Trefftz-based methods for the Helmholtz problem shows that this novel approach results in robust and effective performance.

AMS subject classification: 35J05, 65N12, 65N30, 74J20

Keywords: Helmholtz equation, virtual element method, polygonal meshes, plane waves, ill-conditioning, nonconforming spaces

1 Introduction

Owing to their flexibility in dealing with complex geometries, Galerkin methods based on polytopal grids have been the object of an extensive study over the last years. Among them, we mention the discontinuous Galerkin method [2], the hybridized discontinuous Galerkin method [18], the hybrid high-order method [23], the mimetic finite difference method [12, 33], the high order boundary element method-based finite element method (FEM) [42], and the virtual element method (VEM) [7, 8]. In this paper, we focus on the latter, which, despite its novelty, has already been used in a wide number of problems, including engineering applications.

In comparison to more standard methods, such as the FEM, the VEM has the feature that it is based on spaces of functions that are not known in closed form, but rather are defined elementwise as solutions to local partial differential equations. Although seeming to be a hindrance at a first glance, this property allows for a natural coupling with the Trefftz setting, where the functions in the trial and test spaces belong elementwise to the kernel of the differential operator of the boundary value problem under consideration. The advantage of incorporating properties of the problem solution in the approximating spaces is that, when solving homogeneous problems, less degrees of freedom are needed in order to achieve a given accuracy. As typical of VEM, after defining local approximation spaces, one needs to introduce a set of degrees of freedom that allow to construct a computable method, via proper stabilizations and mappings onto finite dimensional spaces of functions that (a) possess good approximation properties (polynomials, plane waves, . . .) and (b) are explicitly known.

In this paper, we focus on the approximation of solutions to the two dimensional homogeneous Helmholtz problem, which has already been the target of two different VE approaches. The first one [40] is an H^1 -conforming plane wave VEM (PWVEM), which can be interpreted as a partition of unity method [6], the way that the trial and test spaces consist elementwise of plane wave spaces that are eventually glued together by modulating them via a partition of unity. On the other hand, the second and more recent approach is a nonconforming Trefftz-VEM introduced in [37]. The latter

*Faculty of Mathematics, University of Vienna, 1090 Vienna, Austria (lorenzo.mascotto@univie.ac.at, ilaria.perugia@univie.ac.at, alex.pichler@univie.ac.at)

combines the VE technology with the Trefftz setting in a nonconforming fashion (*à la* Crouzeix-Raviart) following the pioneering works on nonconforming VEM for elliptic problems [5, 14] and their extension to other problems [3, 13–15, 25, 34, 36, 46].

This nonconforming Trefftz-VEM, which can be regarded as a generalization of the nonconforming harmonic VEM [36], is “morally” comparable to many other Trefftz methods for the Helmholtz equation such as the ultra weak variational formulation [16], the wave based method [22], discontinuous methods based on Lagrange multipliers [24] and on least square formulation [39], the plane wave discontinuous Galerkin method (PWDG) [27], and the variational theory of complex rays [41]; see [31] for an overview of such methods.

It has to be mentioned that all of the above Trefftz methods are based on fully discontinuous approximation spaces. A peculiarity of the nonconforming Trefftz-VEM is that a “weak” notion (that is, via proper edge L^2 projections) of traces over the skeleton of the polytopal grid is, differently from discontinuous methods, available.

The aim of the present paper is to continue the work begun in [37], where the nonconforming Trefftz-VEM was firstly introduced, an abstract error analysis was carried out, and h -version error estimates were derived. As already mentioned in [37], the original version of the method does not result in good numerical performance, mainly because of the strong ill-conditioning of the local plane wave basis functions.

The scope of this contribution is manifold. After introducing the model problem and extending the original nonconforming Trefftz-VEM in Section 2, we discuss the implementation details of the method in Section 3. We will consider here a more general Helmholtz boundary value problem than originally done in [37], which will be reflected in the definition of the nonconforming Trefftz-VE spaces. Then, numerical results are presented in Section 4, in order to clarify that, *rebus sic stantibus*, the method severely suffers of ill-conditioning. A numerical recipe based on an edgewise orthonormalization procedure to mitigate this strong ill-conditioning is presented in Section 5. Additionally to the fact that the condition number of the resulting global matrix significantly improves, the number of degrees of freedom is reduced without deteriorating the accuracy. To the best of our understanding, such a recipe cannot be directly applied in the framework of DG methods, see Remark 4. After testing the modified version of the method in several experiments, including an acoustic scattering problem, we compare its performance with that of PWVEM and PWDG. The new approach turns out to be very competitive, when compared to existing technologies, especially in the high-order case and when approximating highly oscillatory problems. Moreover, we numerically study the p - and hp -versions of the method, experimentally assessing exponential convergence for analytic and singular solutions in the former and latter cases, respectively.

2 The nonconforming Trefftz virtual element method

In this section, after introducing the notation and presenting the continuous model problem, we recall the nonconforming Trefftz-VEM of [37].

Throughout the paper, we will denote by $H^s(\mathcal{D})$, $\mathcal{D} \subset \mathbb{R}^2$, the Sobolev space of order $s \in \mathbb{N}$ over the complex field \mathbb{C} . For fractional s , the corresponding Sobolev spaces can be defined via interpolation theory, see e.g. [45]. In addition, we will employ the standard notation for sesquilinear forms, norms and seminorms

$$(\cdot, \cdot)_{s, \mathcal{D}}, \quad \|\cdot\|_{s, \mathcal{D}}, \quad |\cdot|_{s, \mathcal{D}}.$$

The model problem we are interested in is a homogeneous Helmholtz boundary value problem with mixed boundary conditions. More precisely, given $\Omega \subset \mathbb{R}^2$ a bounded polygonal domain, we split its boundary $\partial\Omega$ into

$$\partial\Omega = \overline{\Gamma_D} \cup \overline{\Gamma_N} \cup \overline{\Gamma_R}, \quad \Gamma_D \cap \Gamma_N = \emptyset, \quad \Gamma_D \cap \Gamma_R = \emptyset, \quad \Gamma_N \cap \Gamma_R = \emptyset, \quad |\Gamma_R| > 0. \quad (1)$$

The strong formulation of the continuous problem reads

$$\left\{ \begin{array}{l} \text{find } u \in H^1(\Omega) \text{ such that} \\ -\Delta u - k^2 u = 0 \quad \text{in } \Omega \\ u = g_D \quad \text{on } \Gamma_D \\ \nabla u \cdot \mathbf{n}_\Omega = g_N \quad \text{on } \Gamma_N \\ \nabla u \cdot \mathbf{n}_\Omega + ik\theta u = g_R \quad \text{on } \Gamma_R, \end{array} \right. \quad (2)$$

where $k > 0$ is the wave number (with corresponding wave length $\lambda = \frac{2\pi}{k}$), i is the imaginary unit, \mathbf{n}_Ω denotes the unit normal vector on $\partial\Omega$ pointing outside Ω , $\theta \in \{-1, 1\}$, $g_D \in H^{\frac{1}{2}}(\Gamma_D)$, $g_N \in H^{-\frac{1}{2}}(\Gamma_N)$, and $g_R \in H^{-\frac{1}{2}}(\Gamma_R)$.

The corresponding weak formulation reads

$$\left\{ \begin{array}{l} \text{find } u \in V_{g_D} \text{ such that} \\ b(u, v) = \langle F, v \rangle \quad \forall v \in V_0, \end{array} \right. \quad (3)$$

where

$$V_{g_D} := H_{g_D, \Gamma_D}^1(\Omega) = \left\{ v \in H^1(\Omega) : v|_{\Gamma_D} = g_D \right\}, \quad V_0 := H_{0, \Gamma_D}^1(\Omega) = \left\{ v \in H^1(\Omega) : v|_{\Gamma_D} = 0 \right\}$$

and

$$b(u, v) := a(u, v) + ik\theta \int_{\Gamma_R} u \bar{v} \, ds, \quad \langle F, v \rangle := \int_{\Gamma_N} g_N \bar{v} \, ds + \int_{\Gamma_R} g_R \bar{v} \, ds \quad \forall u, v \in H^1(\Omega),$$

with

$$a(u, v) := \int_{\Omega} \nabla u \cdot \overline{\nabla v} \, dx - k^2 \int_{\Omega} u \bar{v} \, dx \quad \forall u, v \in H^1(\Omega).$$

Since we are assuming that $|\Gamma_R| > 0$, see (1), existence and uniqueness of solutions to the problem (2) follow from the Fredholm alternative and a continuation argument.

Theorem 2.1. *Under the assumptions (1) on Ω , problem (2) is uniquely solvable.*

Proof. We first note that the sesquilinear form $b(\cdot, \cdot)$ in (3) is continuous and satisfies a Gårding inequality [38, p.118]. Owing to the Fredholm alternative [38, Thm. 4.11, 4.12], the problem (2) admits a unique solution if and only if the homogeneous adjoint problem to (2) with homogeneous boundary conditions, which is obtained by switching the sign in front of the boundary integral term over Γ_R in $b(u, v)$, admits only the trivial solution 0.

In order to show this, we consider the variational formulation of the homogeneous adjoint problem with homogeneous boundary conditions, we test with $v = u$, and we take the imaginary part, thus deducing $u = 0$ on Γ_R . In particular, also $\nabla u \cdot \mathbf{n}_\Omega = 0$, due to the definition of the impedance trace.

Let now $U \subset \mathbb{R}^2$ be an open, connected set such that $U \cap \partial\Omega = \Gamma_R$ and $\text{meas}(U \setminus \bar{\Omega}) > 0$. We define $\tilde{\Omega} := \Omega \cup U$ and $\tilde{u} : \tilde{\Omega} \rightarrow \mathbb{C}$ as the extension of u by zero in $\tilde{\Omega} \setminus \Omega$. Then \tilde{u} solves a homogeneous Helmholtz equation in $\tilde{\Omega}$; applying the unique continuation principle, see e.g. [4], leads to $\tilde{u} = 0$ in $\tilde{\Omega}$, and therefore $u = 0$ in Ω . \square

We highlight that the existence and the uniqueness of solutions can also be shown for more general Helmholtz-type boundary value problems, see e.g. [28].

Let now \mathcal{T}_n be a decomposition of Ω into polygons $\{K\}$ with mesh size $h := \max_{K \in \mathcal{T}_n} h_K$, where $h_K := \text{diam}(K)$ for all $K \in \mathcal{T}_n$. Further, we introduce \mathcal{E}_n , \mathcal{E}_n^I and \mathcal{E}_n^B , the set of edges, interior edges, and boundary edges of \mathcal{T}_n , respectively. We assume that the boundary edges comply with respect to the decomposition (1), that is, for all boundary edges $e \in \mathcal{E}_n^B$, e is contained in only one amidst Γ_D , Γ_N , and Γ_R . In the sequel, we will use the following notation for the set of ‘‘Dirichlet, Neumann, and impedance (Robin)’’ edges:

$$\mathcal{E}_n^D = \{e \in \mathcal{E}_n^B : e \subseteq \Gamma_D\}, \quad \mathcal{E}_n^N = \{e \in \mathcal{E}_n^B : e \subseteq \Gamma_N\}, \quad \mathcal{E}_n^R = \{e \in \mathcal{E}_n^B : e \subseteq \Gamma_R\}.$$

For any polygon $K \in \mathcal{T}_n$, we denote by \mathcal{E}^K the set of its edges, by \mathbf{x}_K its centroid, and by n_K the cardinality of \mathcal{E}^K . Finally, given any $e \in \mathcal{E}^K$, we denote by \mathbf{x}_e its midpoint, and by h_e its length. The normal unit vector pointing outside K is denoted by \mathbf{n}_K .

Next, we define plane wave spaces in the bulk of the elements of \mathcal{T}_n and on the edges. To this purpose, fix $p = 2q + 1$, $q \in \mathbb{N}$, and let $\{\mathbf{d}_\ell\}_{\ell \in \mathcal{J}}$ be a set of pairwise different and normalized directions, where $\mathcal{J} := \{1, \dots, p\}$. For every $K \in \mathcal{T}_n$ and $\ell \in \mathcal{J}$, we define the local plane wave space on K by

$$\mathbb{P}\mathbb{W}_p(K) := \text{span} \{w_\ell^K, \ell \in \mathcal{J}\}, \quad (4)$$

where $w_\ell^K(\mathbf{x}) := e^{ik\mathbf{d}_\ell \cdot (\mathbf{x} - \mathbf{x}_K)}|_K$ denotes for all $\ell \in \mathcal{J}$ the plane wave centered in \mathbf{x}_K and travelling along the direction \mathbf{d}_ℓ . As q plays the same role as the polynomial degree in the approximation properties of plane wave spaces, we refer to q as *effective plane wave degree*.

Analogously, given any edge $e \in \mathcal{E}_n$, we introduce $\mathbb{P}\mathbb{W}_p(e)$ as the span of the traces of plane waves generating the space $\mathbb{P}\mathbb{W}_p(K)$ on e , namely $w_\ell^e(\mathbf{x}) := e^{ik\mathbf{d}_\ell \cdot (\mathbf{x} - \mathbf{x}_e)}|_e$, $\ell \in \mathcal{J}$.

We note that, in the definition of the bulk and edge plane waves, we also consider a shift by the barycenters of the elements and the midpoints of the edges, respectively. This actually does not change the nature of the basis since it simply results in a multiplication between a nonshifted plane wave with a constant. However, this additional notation may be of help when implementing the method, as it helps to remember when dealing with bulk and/or edge plane waves, see Section 3.

It holds that $\dim(\mathbb{P}\mathbb{W}_p(K)) = p$ for all $K \in \mathcal{T}_n$, but in general $\dim(\mathbb{P}\mathbb{W}_p(e)) \leq p$ for all $e \in \mathcal{E}_n$. In fact, if

$$\mathbf{d}_j \cdot (\mathbf{x} - \mathbf{x}_e) = \mathbf{d}_\ell \cdot (\mathbf{x} - \mathbf{x}_e) \quad \forall \mathbf{x} \in e, \quad (5)$$

for some $j, \ell \in \{1, \dots, p\}$, $j > \ell$, then $w_j^e(\mathbf{x}) = w_\ell^e(\mathbf{x})$ on e .

Thus, in order to avoid the presence of linearly dependent edge plane waves, we have to remove redundant plane waves on the edge e . Further, for theoretical purposes, we also require constant functions to be contained in the edge plane wave spaces in [37]; such choice was instrumental for proving best approximation results in terms of functions in nonconforming Trefftz-VE spaces. Therefore, we add one of the two normal vectors associated with the edge e , whenever it is not already contained in the original set of directions. This whole procedure goes under the name of *filtering process* and was firstly described in [37]. For the sake of completeness, we report it in Algorithm 1. In Figure 1, we depict all possible configurations of distributions of the plane wave directions over the edges.

Algorithm 1 *Filtering process*

For all edges $e \in \mathcal{E}_n$:

1. Remove redundant plane waves

- Initialize $\mathcal{J}'_e := \mathcal{J} := \{1, \dots, p\}$;
- For all indices in \mathcal{J}'_e , check whether (5) is satisfied;
- Whenever this is the case for some pair $j, \ell \in \mathcal{J}'_e$ with $j > \ell$, remove index j from \mathcal{J}'_e ;

2. Add the constants

- Check whether there exists a direction $\mathbf{d}_* \in \{\mathbf{d}_\ell\}_{\ell \in \mathcal{J}}$ such that

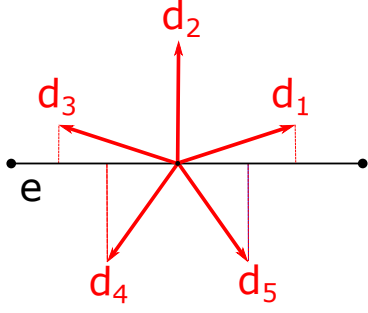
$$\mathbf{d}_* \cdot (\mathbf{x} - \mathbf{x}_e) = 0 \quad \forall \mathbf{x} \in e;$$

- If this is the case, set $\mathcal{J}_e := \mathcal{J}'_e$; otherwise, set $\mathcal{J}_e := \mathcal{J}'_e \cup \{p+1\}$ and $w_{p+1}^e(\mathbf{x}) := 1$.
-

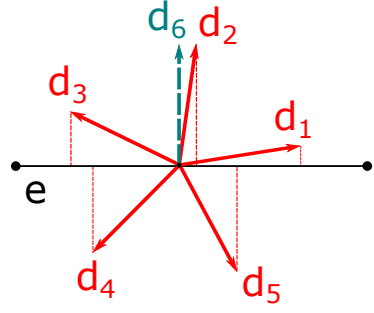
After having performed the filtering process, for every edge $e \in \mathcal{E}_n$, we define

$$\mathbb{P}\mathbb{W}_p^c(e) := \text{span} \{w_\ell^e, \ell \in \mathcal{J}_e\}, \quad (6)$$

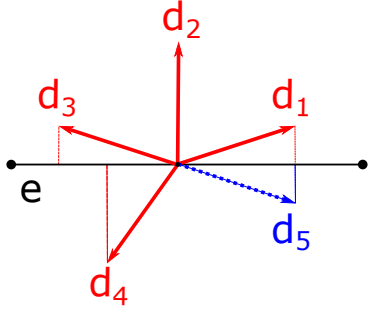
and $p_e := \dim(\mathbb{P}\mathbb{W}_p^c(e)) \leq p + 1$.



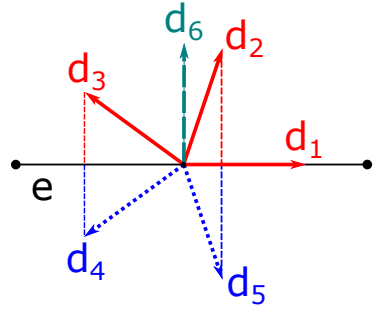
(a) No direction eliminated, orthogonal direction already included.



(b) No direction eliminated, orthogonal direction not included.



(c) One direction eliminated, orthogonal direction already included.



(d) Two directions eliminated, orthogonal direction not included.

Figure 1: Filtering process. We depict all the possible configurations. In solid lines, the directions that are kept; in dotted lines, the directions that are eliminated accordingly with (5); in dashed lines, the orthogonal direction that has to be possibly added in order to include constants.

Next, for any $K \in \mathcal{T}_n$, we introduce the *local* Trefftz-VE space

$$V_h(K) := \{v_h \in H^1(K) \mid \Delta v_h + k^2 v_h = 0 \text{ in } K, \quad v_h|_e \in \mathbb{P}\mathbb{W}_p^c(e) \quad \forall e \in \mathcal{E}^K \cap (\mathcal{E}_n^D \cup \mathcal{E}_n^N), \\ \gamma_I^K(v_h)|_e \in \mathbb{P}\mathbb{W}_p^c(e) \quad \forall e \in \mathcal{E}^K \setminus (\mathcal{E}_n^D \cup \mathcal{E}_n^N)\}, \quad (7)$$

where we have set the element impedance trace $\gamma_I^K(v_h) := \nabla v_h \cdot \mathbf{n}_K + ik\theta v_h$.

Note that it holds $\mathbb{P}\mathbb{W}_p(K) \subset V_h(K)$, but $V_h(K)$ also contains other functions whose explicit representation is not available in closed form. This gives rise to the term *virtual* in the name of the method. For future use, we denote $p_K := \dim(V_h(K)) = \sum_{e \in \mathcal{E}^K} p_e$.

Setting $\mathcal{M}_K := \{1, \dots, n_K\}$, on every $K \in \mathcal{T}_n$, we introduce a set of functionals defined as the moments on each edge $e_r \in \mathcal{E}^K$, $r \in \mathcal{M}_K$, with respect to functions in the space $\mathbb{P}\mathbb{W}_p^c(e_r)$ given in (6):

$$\text{dof}_{r,j}(v_h) := \frac{1}{h_{e_r}} \int_{e_r} v_h \overline{w_j^{e_r}} \, ds \quad \forall r \in \mathcal{M}_K, \forall j \in \mathcal{J}_{e_r}. \quad (8)$$

This set constitutes a set of degrees of freedom, as proven in the forthcoming result.

Lemma 2.2. *Assume that k^2 is not a Dirichlet-Laplace eigenvalue on the element K . Then, the set of functionals in (8) defines a set of unisolvent degrees of freedom for the local space $V_h(K)$ introduced in (7).*

Proof. If $\mathcal{E}^K \cap (\mathcal{E}_n^D \cup \mathcal{E}_n^N) = \emptyset$, the proof is identical to that of [37, Lemma 3.1]. Otherwise, we observe that, if $v_h \in V_h(K)$ is such that all the associated functionals in (8) are zero, then $v_h|_e = 0$ on each edge $e \in \mathcal{E}^K \cap (\mathcal{E}_n^D \cup \mathcal{E}_n^N)$, due to the fact that $v_h|_e \in \mathbb{P}\mathbb{W}_p^c(e)$, together with the definition of the degrees of freedom. This, combined with an integration by parts, leads to

$$|v_h|_{1,K}^2 - k^2 \|v_h\|_{0,K}^2 - ik\theta \|v_h\|_{0,\partial K \setminus (\Gamma_D \cup \Gamma_N)}^2 = \int_{\partial K \setminus (\Gamma_D \cup \Gamma_N)} v_h \overline{\gamma_I^K(v_h)} \, ds = 0.$$

Taking the imaginary part finally gives $v_h = 0$ on $\partial K \setminus (\Gamma_D \cup \Gamma_N)$, and therefore $v_h = 0$ on ∂K . Next, recalling that v_h belongs to the kernel of the Helmholtz operator and k^2 is not a Dirichlet-Laplace eigenvalue, we deduce $v_h = 0$ in K , which is the assertion. \square

Having this, the set of local canonical basis functions $\{\varphi_{s,\ell}\}_{s \in \mathcal{M}_K, \ell \in \mathcal{J}_{e_s}}$ associated with the set of degrees of freedom (8) is defined as

$$\text{dof}_{r,j}(\varphi_{s,\ell}) = \delta_{r,s} \delta_{j,\ell} \quad \forall r, s \in \mathcal{M}_K, \forall j \in \mathcal{J}_{e_r}, \forall \ell \in \mathcal{J}_{e_s}, \quad (9)$$

where δ is the Kronecker delta.

Next, we construct the global Trefftz-VE space, assuming uniform p ; the case when p may vary from element to element is discussed in Section 5.3.3 below. We need to fix some additional notation. Firstly, we define the broken Sobolev space associated with the decomposition \mathcal{T}_n by

$$H^1(\mathcal{T}_n) := \prod_{K \in \mathcal{T}_n} H^1(K) = \{v \in L^2(\Omega) : v|_K \in H^1(K) \quad \forall K \in \mathcal{T}_n\},$$

endowed with the corresponding weighted broken Sobolev norm

$$\|v\|_{1,k,\mathcal{T}_n}^2 := \sum_{K \in \mathcal{T}_n} \|v\|_{1,k,K}^2 = \sum_{K \in \mathcal{T}_n} (|v|_{1,K}^2 + k^2 \|v\|_{0,K}^2).$$

Secondly, we pinpoint the global nonconforming Sobolev space associated with \mathcal{T}_n incorporating in a nonconforming fashion a Dirichlet boundary datum $\tilde{g} \in H^{\frac{1}{2}}(\Gamma_D)$:

$$\begin{aligned} H_{\tilde{g}}^{1,nc}(\mathcal{T}_n) := \{v \in H^1(\mathcal{T}_n) : \int_e (v^+ - v^-) \overline{w^e} ds = 0 \quad \forall w^e \in \mathbb{P}\mathbb{W}_p^c(e), \forall e \in \mathcal{E}_n^I, \\ \int_e (v - \tilde{g}) \overline{w^e} ds = 0 \quad \forall w^e \in \mathbb{P}\mathbb{W}_p^c(e), \forall e \in \mathcal{E}_n^D\}, \end{aligned} \quad (10)$$

where, on each internal edge $e \in \mathcal{E}_n^I$ with $e \subseteq \partial K^- \cap \partial K^+$ for some $K^-, K^+ \in \mathcal{T}_n$, the functions v^- and v^+ are the Dirichlet traces of v from K^- and K^+ , respectively.

The *global* nonconforming Trefftz-VE trial and test spaces are given by

$$V_{h,g_D} = \{v_h \in H_{g_D}^{1,nc}(\mathcal{T}_n) : v_{h|_K} \in V_h(K) \quad \forall K \in \mathcal{T}_n\} \quad (11)$$

and

$$V_{h,0} = \{v_h \in H_0^{1,nc}(\mathcal{T}_n) : v_{h|_K} \in V_h(K) \quad \forall K \in \mathcal{T}_n\}, \quad (12)$$

respectively. In both cases, the set of global degrees of freedom is obtained by coupling the local degrees of freedom on the interfaces between elements.

Remark 1. Owing to the definition (10), the Dirichlet boundary conditions are imposed weakly, via the definition of moments with respect to plane waves. At the computational level, one can approximate g_D by taking a sufficiently high-order Gauß-Lobatto interpolant.

With these ingredients at hand, we recall the construction of the method from [37]. To this purpose, we first fix the notation for the local sesquilinear forms over $K \in \mathcal{T}_n$:

$$a^K(u, v) := \int_K \nabla u \cdot \overline{\nabla v} dx - k^2 \int_K u \overline{v} dx \quad \forall u, v \in H^1(K).$$

Then, for a given $K \in \mathcal{T}_n$, we define the local projector

$$\begin{aligned} \Pi_p^K : V_h(K) &\rightarrow \mathbb{P}\mathbb{W}_p(K) \\ a^K(\Pi_p^K u_h, w^K) &= a^K(u_h, w^K) \quad \forall u_h \in V_h(K), \forall w^K \in \mathbb{P}\mathbb{W}_p(K). \end{aligned} \quad (13)$$

Using an integration by parts, one can observe that Π_p^K is indeed computable without explicit knowledge of the Trefftz-VE functions in the bulk of K , thanks to the choice of the degrees of freedom in (8).

Remark 2. In [37, Proposition 3.2], it was proven that, whenever k^2 is not a Neumann-Laplace eigenvalue in K , the projector Π_p^K in (13) is well-defined and continuous. In order to numerically investigate this condition, we plot the minimal (absolute) eigenvalues of the matrix $\mathbf{A}^{\widehat{K}} := \{a^{\widehat{K}}(w_\ell^{\widehat{K}}, w_j^{\widehat{K}})\}_{\ell, j=1, \dots, p}$ in terms of the wave number k on the reference element $\widehat{K} = (0, 1)^2$, see Figure 2. On this domain, the Neumann-Laplace eigenvalues $\nu_{m,n}$ are known explicitly:

$$\nu_{m,n} = \pi^2(m^2 + n^2), \quad m, n \in \mathbb{N}_0.$$

We observe that, for wave numbers k close to the square roots of the eigenvalues $\nu_{m,n}$, the

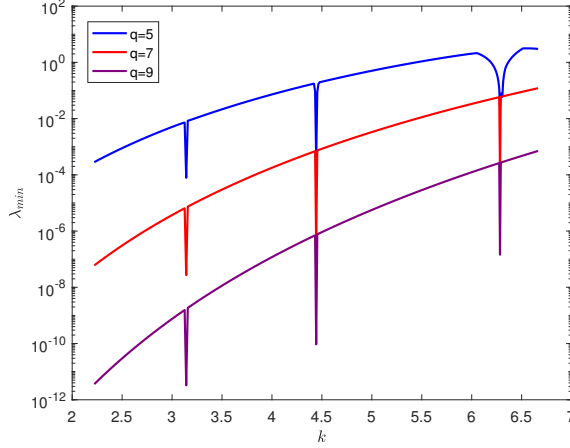


Figure 2: Minimal (absolute) eigenvalues of the matrix $\mathbf{A}^{\widehat{K}}$, see Remark 2.

minimal (absolute) eigenvalue of $\mathbf{A}^{\widehat{K}}$ is actually some orders of magnitude lower than outside the neighborhoods of $\sqrt{\nu_{m,n}}$. Therefore, when k^2 is close to a Neumann-Laplace eigenvalue, the continuity constant of Π_p^K may deteriorate.

On any boundary edge $e \in \mathcal{E}_n^B$, denoting by $K_e \in \mathcal{T}_n$ the adjacent element of e , we further set the $L^2(e)$ projector

$$\begin{aligned} \Pi_p^{0,e} : V_h(K_e)|_e &\rightarrow \mathbb{P}\mathbb{W}_p^c(e) \\ \int_e (\Pi_p^{0,e} u_h) \overline{w^e} \, ds &= \int_e u_h \overline{w^e} \, ds \quad \forall u_h \in V_h(K_e), \forall w^e \in \mathbb{P}\mathbb{W}_p^c(e). \end{aligned} \quad (14)$$

Again by (8), this projector is computable as well. In the sequel, we will use the notation $\Pi_p^{0,\omega}$ to denote the L^2 projector onto the space $\prod_{e \in \omega} \mathbb{P}\mathbb{W}_p^c(e)$ defined edgewise by (14), where ω is either Γ_R or Γ_N .

We highlight that the method is not obtained by simply substituting the spaces V_{gD} and V_0 in (3) by the discrete spaces $V_{h,gD}$ and $V_{h,0}$. In fact, on the one hand, an explicit representation of Trefftz-VE functions is not elementwise available in closed form, and hence $a(u_h, v_h)$ is not computable by means of the degrees of freedom (8) for all $u_h \in V_{h,gD}$ and $v_h \in V_{h,0}$. On the other, Dirichlet traces of Trefftz-VE functions are unknown on Γ_R , see (1), and therefore $\langle F, v_h \rangle$ and the term $ik\theta \int_{\Gamma_R} u_h \overline{v_h} \, ds$ cannot be computed for all $v_h \in V_{h,0}$.

Following the standard VEM gospel [7], we replace the original sesquilinear forms and right-hand sides with some computable counterparts. More precisely:

- (i) In order to find a suitable computable substitute for the sesquilinear form in (3)

$$b(u, v) = \sum_{K \in \mathcal{T}_n} \left[\int_K \nabla u \cdot \overline{\nabla v} \, dx - k^2 \int_K u \overline{v} \, dx \right] + ik \int_{\Gamma_R} u \overline{v} \, ds,$$

we first make use of the definition of the projector Π_p^K in (14), obtaining, for the bulk term,

$$a^K(u_h, v_h) = a^K(\Pi_p^K u_h, \Pi_p^K v_h) + a^K((I - \Pi_p^K)u_h, (I - \Pi_p^K)v_h) \quad \forall u_h, v_h \in V_h(K).$$

The first term on the right-hand side is computable, but the second one is not. Hence, the latter is substituted by a proper computable sesquilinear form $S^K(\cdot, \cdot)$ mimicking $a^K(\cdot, \cdot)$, and referred to in the following as *stabilization*. Therefore, we are able to introduce local discrete sesquilinear forms

$$a_h^K(u_h, v_h) := a^K(\Pi_p^K u_h, \Pi_p^K v_h) + S^K((I - \Pi_p^K)u_h, (I - \Pi_p^K)v_h) \quad \forall u_h, v_h \in V_h(K). \quad (15)$$

In order to guarantee the well-posedness of the method, some conditions on the choice of $S^K(\cdot, \cdot)$ are needed, see [37, Proposition 3.4, Theorem 4.3]. We anticipate that, in Section 5.3.1, we will discuss the effects of the choice of the stabilization on the numerical performance of the method. It is important to mention that the local sesquilinear form is *consistent* in the sense that

$$a_h^K(v_h, w^K) = a^K(v_h, w^K), \quad a_h^K(w^K, v_h) = a^K(w^K, v_h) \quad \forall v_h \in V_h(K), \forall w^K \in \mathbb{P}\mathbb{W}_p(K). \quad (16)$$

The boundary term is instead discretized by

$$ik\theta \int_{\Gamma_R} u\bar{v} \, ds \quad \mapsto \quad ik\theta \int_{\Gamma_R} (\Pi_p^{0, \Gamma_R} u_h) \overline{(\Pi_p^{0, \Gamma_R} v_h)} \, ds \quad \forall u_h \in V_{h, g_D}, \forall v_h \in V_{h, 0}.$$

Altogether, $b(u, v)$ is discretized by

$$b_h(u_h, v_h) := a_h(u_h, v_h) + ik\theta \int_{\Gamma_R} (\Pi_p^{0, \Gamma_R} u_h) \overline{(\Pi_p^{0, \Gamma_R} v_h)} \, ds \quad \forall u_h \in V_{h, g_D}, \forall v_h \in V_{h, 0}, \quad (17)$$

with

$$a_h(u_h, v_h) := \sum_{K \in \mathcal{T}_n} a_h^K(u_h, v_h) \quad \forall u_h \in V_{h, g_D}, \forall v_h \in V_{h, 0}. \quad (18)$$

(ii) The functional

$$\langle F, v \rangle = \int_{\Gamma_N} g_N \bar{v} \, ds + \int_{\Gamma_R} g_R \bar{v} \, ds$$

on the right-hand side of (3) is discretized by

$$\langle F_h, v_h \rangle := \int_{\Gamma_N} g_N \overline{(\Pi_p^{0, \Gamma_N} v_h)} + \int_{\Gamma_R} g_R \overline{(\Pi_p^{0, \Gamma_R} v_h)} \, ds \quad v_h \in V_{h, 0}. \quad (19)$$

With these definitions, the nonconforming Trefftz-VEM reads as follows:

$$\begin{cases} \text{find } u_h \in V_{h, g_D} \text{ such that} \\ b_h(u_h, v_h) = \langle F_h, v_h \rangle \quad \forall v_h \in V_{h, 0}, \end{cases} \quad (20)$$

where $b_h(\cdot, \cdot)$ and $\langle F_h, \cdot \rangle$ are given in (17) and (19), respectively.

In [37], an abstract error analysis of the method (20), along with h -convergence results, was proven for the case that $\Gamma_R = \partial\Omega$.

3 Details on the implementation

In this section, we give some details concerning the implementation of the method (20), involving in particular the computation of the two projectors Π_p^K and $\Pi_p^{0, e}$ introduced in (13) and (14), respectively. We point out that, despite the setting of the method (20) is rather different from that of standard VEM, the implementation follows the same lines; hence, we will employ the same ideas and notation as in [8].

3.1 Assembly of the global system of linear equations

The global system of linear equations corresponding to the method (20) is assembled as in the standard nonconforming VEM [5, 36] and FEM [20]. For the sake of clarity, we first consider the case that $\Gamma_D = \emptyset$. The general case will be addressed in Section 3.5 below.

Given N_e the total number of edges of the mesh \mathcal{T}_n , let $\{\varphi_{\tilde{s}, \tilde{\ell}}\}_{\tilde{s}=1, \dots, N_e, \tilde{\ell} \in \mathcal{J}_{e_{\tilde{s}}}}$ be the set of canonical basis functions given by (9). In this section, we use the convention that the indices hooded by a tilde denote global indices, whereas those without stand for local ones.

Expanding u_h as $\sum_{\tilde{s}=1}^{N_e} \sum_{\tilde{\ell}=1}^{p_{e_{\tilde{s}}}} u_{\tilde{s}, \tilde{\ell}} \varphi_{\tilde{s}, \tilde{\ell}}$ and plugging this ansatz into (20) lead to

$$\begin{aligned} & \sum_{\tilde{s}=1}^{N_e} \sum_{\tilde{\ell}=1}^{p_{e_{\tilde{s}}}} u_{\tilde{s}, \tilde{\ell}} \left[a_h(\varphi_{\tilde{s}, \tilde{\ell}}, \varphi_{\tilde{r}, \tilde{j}}) + ik\theta \int_{\Gamma_R} (\Pi_p^{0, \Gamma_R} \varphi_{\tilde{s}, \tilde{\ell}}) \overline{(\Pi_p^{0, \Gamma_R} \varphi_{\tilde{r}, \tilde{j}})} ds \right] \\ &= \int_{\Gamma_N} g_N \overline{(\Pi_p^{0, \Gamma_N} \varphi_{\tilde{r}, \tilde{j}})} + \int_{\Gamma_R} g_R \overline{(\Pi_p^{0, \Gamma_R} \varphi_{\tilde{r}, \tilde{j}})} ds \quad \forall \tilde{r} = 1, \dots, N_e, \forall \tilde{j} = 1, \dots, p_{e_{\tilde{r}}}, \end{aligned} \quad (21)$$

where, with a slight abuse of notation, we relabelled by $1, \dots, p_{e_{\tilde{s}}}$ the indices in $\mathcal{J}_{e_{\tilde{s}}}$ that remain after the filtering process similarly for the ones in $\mathcal{J}_{e_{\tilde{r}}}$.

We observe that (21) can be represented as the linear system

$$(\mathbf{A} + \mathbf{R})\mathbf{u} = \mathbf{f}, \quad (22)$$

where $\mathbf{A}, \mathbf{R} \in \mathbb{C}^{N_{\text{dof}} \times N_{\text{dof}}}$, $\mathbf{u} \in \mathbb{C}^{N_{\text{dof}}}$, and $\mathbf{f} \in \mathbb{C}^{N_{\text{dof}}}$, N_{dof} being the total number of global degrees of freedom, are matrices and vectors with entries defined by

$$\begin{aligned} \mathbf{A}_{(\tilde{r}, \tilde{j}), (\tilde{s}, \tilde{\ell})} &= a_h(\varphi_{\tilde{s}, \tilde{\ell}}, \varphi_{\tilde{r}, \tilde{j}}), & \mathbf{R}_{(\tilde{r}, \tilde{j}), (\tilde{s}, \tilde{\ell})} &= ik\theta \int_{\Gamma_R} (\Pi_p^{0, \Gamma_R} \varphi_{\tilde{s}, \tilde{\ell}}) \overline{(\Pi_p^{0, \Gamma_R} \varphi_{\tilde{r}, \tilde{j}})} ds, \\ \mathbf{u}_{(\tilde{s}, \tilde{\ell})} &= u_{\tilde{s}, \tilde{\ell}}, & \mathbf{f}_{(\tilde{r}, \tilde{j})} &= \int_{\Gamma_N} g_N \overline{(\Pi_p^{0, \Gamma_N} \varphi_{\tilde{r}, \tilde{j}})} + \int_{\Gamma_R} g_R \overline{(\Pi_p^{0, \Gamma_R} \varphi_{\tilde{r}, \tilde{j}})} ds. \end{aligned}$$

Note that here the subindex (\tilde{r}, \tilde{j}) is associated with the index $\sum_{\tilde{i}=1}^{\tilde{r}-1} p_{e_{\tilde{i}}} + \tilde{j}$. The computation of \mathbf{A} , \mathbf{R} , and \mathbf{f} are described in the forthcoming Sections 3.2, 3.3, and 3.4, respectively.

3.2 Computation of the matrix \mathbf{A}

Using the definition of $a_h(\cdot, \cdot)$ in (18), together with (15), we have

$$\mathbf{A}_{(\tilde{r}, \tilde{j}), (\tilde{s}, \tilde{\ell})} = a_h(\varphi_{\tilde{s}, \tilde{\ell}}, \varphi_{\tilde{r}, \tilde{j}}) = \sum_{K \in \mathcal{T}_n} \left[a^K (\Pi_p^K \varphi_{\tilde{s}, \tilde{\ell}}, \Pi_p^K \varphi_{\tilde{r}, \tilde{j}}) + S^K \left((I - \Pi_p^K) \varphi_{\tilde{s}, \tilde{\ell}}, (I - \Pi_p^K) \varphi_{\tilde{r}, \tilde{j}} \right) \right]. \quad (23)$$

The global matrix \mathbf{A} is then assembled by means of the local matrices $\mathbf{A}^K \in \mathbb{C}^{p_K \times p_K}$ that are defined as

$$\mathbf{A}_{(r, j), (s, \ell)}^K = a^K (\Pi_p^K \varphi_{s, \ell}, \Pi_p^K \varphi_{r, j}) + S^K \left((I - \Pi_p^K) \varphi_{s, \ell}, (I - \Pi_p^K) \varphi_{r, j} \right),$$

where $\{\varphi_{s, \ell}\}_{s \in \mathcal{M}_K, \ell \in \mathcal{J}_{e_s}}$ denotes the local basis of $V_h(K)$.

Following [8], the computation of such local matrices is performed in various steps.

Computation of the bulk projector Π_p^K in (13). Let $\varphi_{s, \ell} \in V_h(K)$, $s \in \mathcal{M}_K$, $\ell \in \mathcal{J}_{e_s}$, be the canonical basis function. As a first step, we write $\Pi_p^K \varphi_{s, \ell} \in \mathbb{P}\mathbb{W}_p(K)$ as a linear combination of the plane waves $w_\zeta^K \in \mathbb{P}\mathbb{W}_p(K)$, $\zeta = 1, \dots, p$,

$$\Pi_p^K \varphi_{s, \ell} = \sum_{\zeta=1}^p \gamma_\zeta^{K(s, \ell)} w_\zeta^K.$$

Plugging this ansatz into (13) and testing with plane waves lead to the system of linear equations

$$\mathbf{G}^K \boldsymbol{\gamma}^{K(s, \ell)} = \mathbf{b}^{K(s, \ell)},$$

where $\mathbf{G}^K \in \mathbb{C}^{p \times p}$, $\boldsymbol{\gamma}^{K(s,\ell)} \in \mathbb{C}^p$, $\mathbf{b}^{K(s,\ell)} \in \mathbb{C}^p$, for all $s \in \mathcal{M}_K$ and $\ell \in \mathcal{J}_{e_s}$, are defined as

$$\mathbf{G}^K := \begin{bmatrix} a^K(w_1^K, w_1^K) & \cdots & a^K(w_p^K, w_1^K) \\ \vdots & \ddots & \vdots \\ a^K(w_1^K, w_p^K) & \cdots & a^K(w_p^K, w_p^K) \end{bmatrix}, \quad \boldsymbol{\gamma}^{K(s,\ell)} := \begin{bmatrix} \gamma_1^{K(s,\ell)} \\ \vdots \\ \gamma_p^{K(s,\ell)} \end{bmatrix}, \quad \mathbf{b}^{K(s,\ell)} := \begin{bmatrix} a^K(\varphi_{s,\ell}, w_1^K) \\ \vdots \\ a^K(\varphi_{s,\ell}, w_p^K) \end{bmatrix}.$$

Collecting columnwise the $\mathbf{b}^{K(s,\ell)}$ leads to a matrix $\mathbf{B}^K := [\mathbf{b}^{K(1,1)}, \dots, \mathbf{b}^{K(n_K, p_{e_{n_K}})}] \in \mathbb{C}^{p \times p_K}$.

The matrix $\boldsymbol{\Pi}_*^K$ representing the action of Π_p^K from $V_h(K)$ into $\mathbb{P}\mathbb{W}_p(K)$ is then given by

$$\boldsymbol{\Pi}_*^K = (\mathbf{G}^K)^{-1} \mathbf{B}^K \in \mathbb{C}^{p \times p_K}. \quad (24)$$

We introduce next the matrix

$$\mathbf{D}^K := \begin{bmatrix} \text{dof}_{1,1}(w_1^K) & \cdots & \text{dof}_{1,1}(w_p^K) \\ \vdots & \ddots & \vdots \\ \text{dof}_{n_K, p_{e_{n_K}}}(w_1^K) & \cdots & \text{dof}_{n_K, p_{e_{n_K}}}(w_p^K) \end{bmatrix} \in \mathbb{C}^{p_K \times p}.$$

Then, as in [8], the matrix $\boldsymbol{\Pi}^K$ representing the composition of the embedding of $\mathbb{P}\mathbb{W}_p(K)$ into $V_h(K)$ after $\boldsymbol{\Pi}_*^K$ can be expressed as

$$\boldsymbol{\Pi}^K = \mathbf{D}^K (\mathbf{G}^K)^{-1} \mathbf{B}^K \in \mathbb{C}^{p_K \times p_K}. \quad (25)$$

Matrix representation of $\mathbf{A}^K \in \mathbb{C}^{p_K \times p_K}$. The local VE stiffness matrix \mathbf{A}^K is given by

$$\mathbf{A}^K = \overline{(\boldsymbol{\Pi}_*^K)^T} \mathbf{G}^K \boldsymbol{\Pi}_*^K + \overline{(\mathbf{I}^K - \boldsymbol{\Pi}^K)^T} \mathbf{S}^K (\mathbf{I}^K - \boldsymbol{\Pi}^K), \quad (26)$$

where \mathbf{I}^K denotes the identity matrix of size $p_K \times p_K$, and \mathbf{S}^K is the matrix representation of the local stabilization forms $S^K(\cdot, \cdot)$; for a specific choice of the stabilization, we refer to Section 5.3 below. Further, note that by using (24), it holds

$$\overline{(\boldsymbol{\Pi}_*^K)^T} \mathbf{G}^K \boldsymbol{\Pi}_*^K = \overline{(\mathbf{B}^K)^T} (\mathbf{G}^K)^{-T} \mathbf{B}^K.$$

3.2.1 Computation of the local matrices \mathbf{G}^K , \mathbf{B}^K , and \mathbf{D}^K

The matrices \mathbf{G}^K , \mathbf{B}^K , and \mathbf{D}^K can actually be computed exactly without numerical integration, but rather by using the definition of the degrees of freedom in (8) and the formula

$$\Phi(z) := \int_0^1 e^{zt} dt = \begin{cases} \frac{e^z - 1}{z} & \text{if } z \neq 0 \\ 1 & \text{if } z = 0 \end{cases} \quad \forall z \in \mathbb{C}. \quad (27)$$

This has been already investigated in [26, 40].

Computation of $\mathbf{G}^K \in \mathbb{C}^{p \times p}$. Given $j, \ell \in \mathcal{J}$, we compute, by using an integration by parts and taking into account the definition of the bulk plane waves w_j^K and w_ℓ^K , respectively,

$$\begin{aligned} \mathbf{G}_{j,\ell}^K &= a^K(w_\ell^K, w_j^K) = \sum_{r=1}^{n_K} \int_{e_r} (\nabla w_\ell^K \cdot \mathbf{n}_{K|e_r}) \overline{w_j^K} ds \\ &= ik \sum_{r=1}^{n_K} e^{ik(\mathbf{d}_j - \mathbf{d}_\ell) \cdot \mathbf{x}_K} (\mathbf{d}_\ell \cdot \mathbf{n}_{K|e_r}) \int_{e_r} e^{ik(\mathbf{d}_\ell - \mathbf{d}_j) \cdot \mathbf{x}} ds. \end{aligned}$$

The integral over the edges e_r , $r \in \mathcal{M}_K$, on the right-hand side can be computed by application of the transformation rule. In fact, denoting by \mathbf{a}_r and \mathbf{b}_r the endpoints of the edge e_r , we obtain

$$\begin{aligned} \int_{e_r} e^{ik(\mathbf{d}_\ell - \mathbf{d}_j) \cdot \mathbf{x}} ds &= h_{e_r} e^{ik(\mathbf{d}_\ell - \mathbf{d}_j) \cdot \mathbf{a}_r} \int_0^1 e^{ik(\mathbf{d}_\ell - \mathbf{d}_j) \cdot (\mathbf{b}_r - \mathbf{a}_r)t} dt \\ &= h_{e_r} e^{ik(\mathbf{d}_\ell - \mathbf{d}_j) \cdot \mathbf{a}_r} \Phi(ik(\mathbf{d}_\ell - \mathbf{d}_j) \cdot (\mathbf{b}_r - \mathbf{a}_r)), \end{aligned} \quad (28)$$

where Φ is defined in (27).

Computation of $B^K \in \mathbb{C}^{p \times p_K}$. Given $s \in \mathcal{M}_K$, $\ell \in \mathcal{J}_{e_s}$, $j \in \mathcal{J}$, an integration by parts, the definitions of the local canonical basis functions in (9), and the definition of the degrees of freedom in (8) yield

$$\begin{aligned} B_{j,(s,\ell)}^K &= a^K(\varphi_{s,\ell}, w_j^K) = \sum_{r=1}^{n_K} \int_{e_r} \varphi_{s,\ell} \overline{(\nabla w_j^K \cdot \mathbf{n}_{K|e_r})} ds = -ik \sum_{r=1}^{n_K} (\mathbf{d}_j \cdot \mathbf{n}_{K|e_r}) \int_{e_r} \varphi_{s,\ell} \overline{w_j^K} ds \\ &= -ik (\mathbf{d}_j \cdot \mathbf{n}_{K|e_s}) e^{-ik \mathbf{d}_j \cdot (\mathbf{x}_{e_s} - \mathbf{x}_K)} \int_{e_s} \varphi_{s,\ell} \underbrace{e^{ik \mathbf{d}_j \cdot (\mathbf{x} - \mathbf{x}_{e_s})}}_{=w_t^{e_s}} ds \\ &= -ik (\mathbf{d}_j \cdot \mathbf{n}_{K|e_s}) e^{-ik \mathbf{d}_j \cdot (\mathbf{x}_{e_s} - \mathbf{x}_K)} h_{e_s} \delta_{t,\ell}. \end{aligned}$$

where $t \in \mathcal{J}_{e_s}$ is the local index such that $w_t^{e_s} = e^{ik \mathbf{d}_j \cdot (\mathbf{x} - \mathbf{x}_{e_s})}$ on e_s .

Computation of $D^K \in \mathbb{C}^{p_K \times p}$. Given $r \in \mathcal{M}_K$, $j \in \mathcal{J}_{e_r}$, $\ell \in \mathcal{J}$, a direct computation gives

$$\text{dof}_{r,j}(w_\ell^K) = \frac{1}{h_{e_r}} \int_{e_r} w_\ell^K \overline{w_j^{e_r}} ds = \frac{1}{h_{e_r}} e^{ik(\mathbf{d}_j \cdot \mathbf{x}_{e_r} - \mathbf{d}_\ell \cdot \mathbf{x}_K)} \int_{e_r} e^{ik(\mathbf{d}_\ell - \mathbf{d}_j) \cdot \mathbf{x}} ds.$$

The last term on the right-hand side can be computed as in (28).

3.3 Computation of the Robin boundary matrix R

Recall that the Robin boundary matrix R is given by

$$\mathbf{R}_{(\tilde{r},\tilde{j}),(\tilde{s},\tilde{\ell})} = ik\theta \sum_{e \in \mathcal{E}_n^R} \int_e (\Pi_p^{0,e} \varphi_{\tilde{s},\tilde{\ell}}) \overline{(\Pi_p^{0,e} \varphi_{\tilde{r},\tilde{j}})} ds. \quad (29)$$

Similarly as above, the global matrix R is assembled by means of the local matrices $R^e \in \mathbb{C}^{p_e \times p_e}$ that are defined as

$$\mathbf{R}_{(r,j),(s,\ell)}^e = ik\theta \int_e (\Pi_p^{0,e} \varphi_{s,\ell}) \overline{(\Pi_p^{0,e} \varphi_{r,j})} ds,$$

where $\{\varphi_{s,\ell}\}_{s \in \mathcal{M}_K, \ell \in \mathcal{J}_{e_s}}$ denotes the local basis of $V_h(K)$, with K such that $e \subset \partial K \cap \Gamma_R$.

Let $e \in \mathcal{E}_n^R$ be a fixed boundary edge in \mathcal{E}_n^R with local index $z \in \mathcal{M}_K$, where $K \in \mathcal{T}_n$ is the unique polygon with $e = \partial K \cap \Gamma_R$.

Computation of the edge projector $\Pi_p^{0,e}$ in (14). Let $\varphi_{z,\ell} \in V_h(K)$, $\ell \in \mathcal{J}_e$, be a fixed function of the local canonical basis. We first expand $\Pi_p^{0,e} \varphi_{z,\ell} \in \mathbb{P}\mathbb{W}_p^c(e)$ in terms of $w_\eta^e \in \mathbb{P}\mathbb{W}_p^c(e)$, $\eta = 1, \dots, p_e$,

$$\Pi_p^{0,e} \varphi_{z,\ell} = \sum_{\eta=1}^{p_e} \beta_\eta^{e(\ell)} w_\eta^e.$$

Inserting this ansatz into (14) and testing with edge plane waves lead to the linear system

$$\mathbf{G}_0^e \boldsymbol{\beta}^{e(\ell)} = \mathbf{b}_0^{e(\ell)}.$$

Here, $\mathbf{G}_0^e \in \mathbb{C}^{p_e \times p_e}$, $\boldsymbol{\beta}^{e(\ell)} \in \mathbb{C}^{p_e}$, $\mathbf{b}_0^{e(\ell)} \in \mathbb{C}^{p_e}$ for all $\ell \in \mathcal{J}_e$, are defined as

$$\mathbf{G}_0^e := \begin{bmatrix} (w_1^e, w_1^e)_{0,e} & \cdots & (w_{p_e}^e, w_1^e)_{0,e} \\ \vdots & \ddots & \vdots \\ (w_1^e, w_{p_e}^e)_{0,e} & \cdots & (w_{p_e}^e, w_{p_e}^e)_{0,e} \end{bmatrix}, \quad \boldsymbol{\beta}^{e(\ell)} := \begin{bmatrix} \beta_1^{e(\ell)} \\ \vdots \\ \beta_{p_e}^{e(\ell)} \end{bmatrix}, \quad \mathbf{b}_0^{e(\ell)} := \begin{bmatrix} (\varphi_{z,\ell}, w_1^e)_{0,e} \\ \vdots \\ (\varphi_{z,\ell}, w_{p_e}^e)_{0,e} \end{bmatrix}, \quad (30)$$

where $(\cdot, \cdot)_e$ denotes the complex L^2 inner product over e . Note that in fact $\mathbf{G}_0^e \in \mathbb{R}^{p_e \times p_e}$, see (32) below. Moreover, such matrix is positive definite for all $K \in \mathcal{T}_n$, and thus also invertible. Nevertheless, it is worth to underline that in presence of small-sized elements and of a large number of plane waves, such matrix may become singular in machine precision. This problem will be analyzed in Section 4 and addressed in Section 5.

Consequently, collecting the $\mathbf{b}_0^{e(\ell)}$ columnwise into a matrix $\mathbf{B}_0^e \in \mathbb{C}^{p_e \times p_K}$, the matrix representation of $\Pi_p^{0,e}$ is given by

$$\Pi_{\star}^{0,e} = (\mathbf{G}_0^e)^{-1} \mathbf{B}_0^e.$$

Matrix representation of \mathbf{R}^e . The local edge VE boundary mass matrix \mathbf{R}^e has the form

$$\mathbf{R}^e = \overline{\Pi_\star^{0,e}}^T \mathbf{G}_0^e \Pi_\star^{0,e} = \overline{\mathbf{B}_0^e}^T (\overline{\mathbf{G}_0^e})^{-T} \mathbf{B}_0^e. \quad (31)$$

3.3.1 Computation of the local matrices \mathbf{G}_0^e and \mathbf{B}_0^e

The matrices \mathbf{G}_0^e and \mathbf{B}_0^e can be computed exactly using the formula (27).

Computation of $\mathbf{G}_0^e \in \mathbb{R}^{p_e \times p_e}$. Given $j, \ell \in \mathcal{J}_e$ and denoting by \mathbf{a} and \mathbf{b} the endpoints of the edge e , it holds $(\mathbf{G}_0^e)_{j,j} = h_e$ and, if $j \neq \ell$,

$$(\mathbf{G}_0^e)_{j,\ell} = (w_\ell^e, w_j^e)_{0,e} = e^{ik(\mathbf{d}_j - \mathbf{d}_\ell) \cdot \mathbf{x}_e} \int_e e^{ik(\mathbf{d}_\ell - \mathbf{d}_j) \cdot \mathbf{x}} ds = 2h_e \frac{\sin(k(\mathbf{d}_\ell - \mathbf{d}_j) \cdot \frac{\mathbf{b} - \mathbf{a}}{2})}{k(\mathbf{d}_\ell - \mathbf{d}_j) \cdot (\mathbf{b} - \mathbf{a})} \in \mathbb{R}, \quad (32)$$

where we used (28) and the property $\sin(z) = \frac{1}{2i}(e^{iz} - e^{-iz})$, $z \in \mathbb{C}$, in the last equality.

Computation of $\mathbf{B}_0^e \in \mathbb{C}^{p_e \times p_e}$. For all $j, \ell \in \mathcal{J}_e$, the definition of the degrees of freedom in (8) implies

$$(\mathbf{B}_0^e)_{j,\ell} = (\varphi_{z,\ell}, w_j^e)_{0,e} = \int_e \varphi_{z,\ell} \overline{w_j^e} ds = h_e \delta_{j,\ell}.$$

3.4 Computation of the right-hand side vector \mathbf{f}

Recall that \mathbf{f} is given by

$$\mathbf{f}_{(\tilde{r}, \tilde{j})} = \sum_{e \in \mathcal{E}_n^N} \int_e g_N(\overline{\Pi_p^{0,e} \varphi_{\tilde{r}, \tilde{j}}}) ds + \sum_{e \in \mathcal{E}_n^R} \int_e g_R(\overline{\Pi_p^{0,e} \varphi_{\tilde{r}, \tilde{j}}}) ds := \mathbf{f}_{(\tilde{r}, \tilde{j})}^N + \mathbf{f}_{(\tilde{r}, \tilde{j})}^R.$$

Once again, the global right-hand side \mathbf{f} is assembled by means of the local vectors $\mathbf{f}^{N,e} \in \mathbb{C}^{p_e}$ and $\mathbf{f}^{R,e} \in \mathbb{C}^{p_e}$ that are defined as

$$\mathbf{f}_{(r,j)}^{N,e} = \int_e g_N(\overline{\Pi_p^{0,e} \varphi_{r,j}}) ds, \quad \mathbf{f}_{(r,j)}^{R,e} = \int_e g_R(\overline{\Pi_p^{0,e} \varphi_{r,j}}) ds,$$

where $\{\varphi_{s,\ell}\}_{s \in \mathcal{M}_K, \ell \in \mathcal{J}_{e_s}}$ denotes the local basis of $V_h(K)$, with K such that either $e \subset \partial K \cap \Gamma_N$ or $e \subset \partial K \cap \Gamma_R$.

We only show the details concerning the computation of $\mathbf{f}^{N,e}$. The assembly of $\mathbf{f}^{R,e}$ is analogous.

Let therefore $e \in \mathcal{E}_n^N$ be a fixed Neumann boundary edge with local index $z \in \mathcal{M}_K$, where $K \in \mathcal{T}_n$ is the unique polygon with $e = \partial K \cap \Gamma_N$. Then, for every $\ell \in \mathcal{J}_e$, denoting by \mathbf{a}_z and \mathbf{b}_z the endpoints of edge e , we have

$$\begin{aligned} \mathbf{f}_j^{N,e} &= \int_e g_N(\overline{\Pi_p^{0,e} \varphi_{z,j}}) ds = \sum_{\eta=1}^{p_e} \overline{\beta_\eta^{e(j)}} \int_e g_N \overline{w_\eta^e} ds \\ &= \sum_{\eta=1}^{p_e} \overline{\beta_\eta^{e(j)}} h_e \int_0^1 g_N(\mathbf{a}_z + t(\mathbf{b}_z - \mathbf{a}_z)) e^{-ik\mathbf{d}_j \cdot (\mathbf{a}_z + t(\mathbf{b}_z - \mathbf{a}_z) - \mathbf{x}_e)} dt. \end{aligned} \quad (33)$$

The last integral can be approximated employing a Gauß-Lobatto quadrature formula. We remark that the computation of the right-hand side \mathbf{f} is the only one where numerical quadrature may be required.

3.5 General case ($\Gamma_D \neq \emptyset$)

The general case with $\Gamma_D \neq \emptyset$ can be dealt with in a similar fashion. First of all, we implement the global matrices \mathbf{A} , \mathbf{R} and the right-hand side vector \mathbf{f} as above. Then, in order to incorporate the Dirichlet boundary conditions, we additionally impose that the numerical solution u_h satisfies

$$\int_{e_\zeta} (u_h - g_D) \overline{w_j^e} ds = 0 \quad \forall j = 1, \dots, p_{e_\zeta}, \forall e_\zeta \in \mathcal{E}_n^D,$$

which, using the expansion of u_h in terms of the canonical basis functions, leads to

$$\sum_{\tilde{s}=1}^{N_e} \sum_{\tilde{\ell}=1}^{p_{e_{\tilde{s}}}} u_{\tilde{s}, \tilde{\ell}} \int_{e_\zeta} \varphi_{\tilde{s}, \tilde{\ell}} \overline{w_j^{e_\zeta}} ds = \int_{e_\zeta} g_D \overline{w_j^{e_\zeta}} ds \quad \forall j = 1, \dots, p_{e_\zeta}, \forall e_\zeta \in \mathcal{E}_n^D.$$

Employing the definition of the canonical basis functions in (9) and the degrees of freedom in (8) results in

$$u_{\zeta, j} = \frac{1}{h_{e_\zeta}} \int_{e_\zeta} g_D \overline{w_j^{e_\zeta}} ds \quad \forall j = 1, \dots, p_{e_\zeta}, \forall e_\zeta \in \mathcal{E}_n^D. \quad (34)$$

This information is inserted in the linear system (22) by setting to zero all the entries in the rows of \mathbf{A} corresponding to test functions associated with Dirichlet boundary edges, apart from the diagonal entry, which is set to one, and replacing the corresponding values of the vector \mathbf{f} with the right-hand sides of (34).

4 The curse of ill-conditioning

In this section, we investigate the numerical performance of the method (20). We anticipate that the present construction of the method does not deliver accurate results due to the strong ill-conditioning related to the plane wave bases. Therefore, we will propose a numerical recipe apt to remove such instabilities, see Section 5.1 below. All the tests were performed with `Matlab R2016b`.

We consider here boundary value problems of the form (3) with $\theta = 1$, $\Gamma_R = \partial\Omega$ on the square domain $\Omega := (0, 1)^2$ with analytical solutions

$$\begin{aligned} u_0(x, y) &:= \exp(ikx), \\ u_1(x, y) &:= \exp\left(ik\left(\cos\left(\frac{\pi}{4}\right)x + \sin\left(\frac{\pi}{4}\right)y\right)\right). \end{aligned} \quad (35)$$

The functions u_0 and u_1 are plane waves travelling in the directions $(1, 0)$ and $(\frac{\pi}{4}, \frac{\pi}{4})$, respectively, see also Figure 3 for contour plots of the real parts of u_0 and u_1 for $k = 20$.

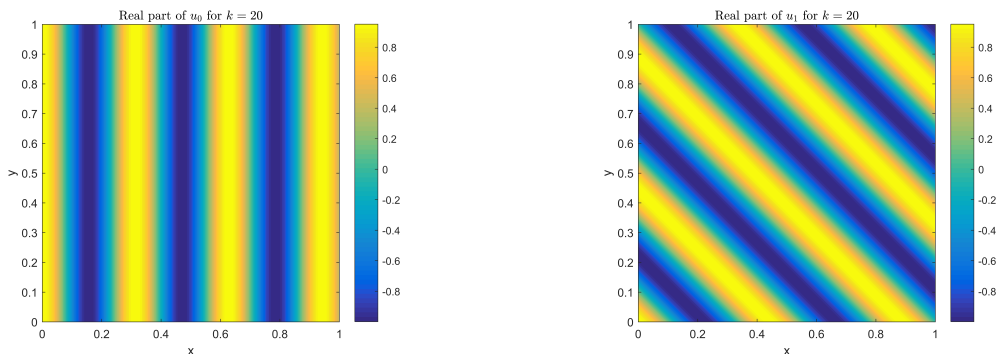


Figure 3: Real parts of the functions u_0 (left) and u_1 (right) defined in (35) for $k = 20$.

Since an exact representation of the numerical solution u_h is not available in closed form inside each element, it is not possible to compute the exact H^1 and L^2 discretization errors directly. Instead, we compute the approximate relative errors

$$\frac{\|u - \Pi_p u_h\|_{1,k,\mathcal{T}_n}}{\|u\|_{1,k,\Omega}}, \quad \frac{\|u - \Pi_p u_h\|_{0,\mathcal{T}_n}}{\|u\|_{0,\Omega}}, \quad (36)$$

where $\Pi_{p|K} = \Pi_p^K$, $K \in \mathcal{T}_n$, is the local projector defined in (13). Mimicking what done in [36], it is possible to show that these relative errors converge with the same rate as the exact relative H^1 and L^2 discretization errors.

Furthermore, we employ two different local stabilizations, which in matrix form read as follows:

- the identity stabilization

$$\mathbf{S}^K = \mathbf{I}^K, \quad (37)$$

where $\mathbf{I}^K \in \mathbb{C}^{p_K \times p_K}$ denotes the identity matrix;

- the *modified D-recipe* stabilization

$$\mathbf{S}_{(s,\ell),(r,j)}^K = \max\{\operatorname{Re}(a^K(\Pi_p^K \varphi_{r,j}, \Pi_p^K \varphi_{s,\ell})), 1\} \delta_{r,s} \delta_{\ell,j}, \quad (38)$$

where δ denotes the Kronecker delta.

The former choice is the original VEM stabilization proposed in [7, 8], whereas the latter is a modification of the *diagonal recipe* (D-recipe), which was introduced in [11], and whose performance was investigated for high-order VEM and in presence of badly-shaped elements in [21, 35].

In order to build a basis of $\mathbb{P}\mathbb{W}_p(K)$, see (4), we employ a set $\{\mathbf{d}_\ell^{(0)}\}_{\ell=1}^p$ of $p = 2q + 1$, $q \in \mathbb{N}$, equidistributed plane wave directions given by

$$\mathbf{d}_\ell^{(0)} = \left(\cos\left(\frac{2\pi}{p}(\ell-1)\right), \sin\left(\frac{2\pi}{p}(\ell-1)\right) \right). \quad (39)$$

We discretize the boundary value problem on sequences of quasi-uniform Cartesian meshes and Voronoi-Lloyd meshes [44], see Figure 4, and investigate the h -version of the method for a fixed wave number $k = 10$ and different values of $q = 2, 3$, and 4. Note that in the case of u_0 , since $u_0 \in \operatorname{span}\{w_\ell^K\}_{\ell=1}^p$ and owing to the consistency property (16) of the discrete bilinear form, the method should reproduce, up to machine precision, the exact solution. The approximate relative L^2 bulk errors defined in (36) are plotted in Figures 5 and 6.

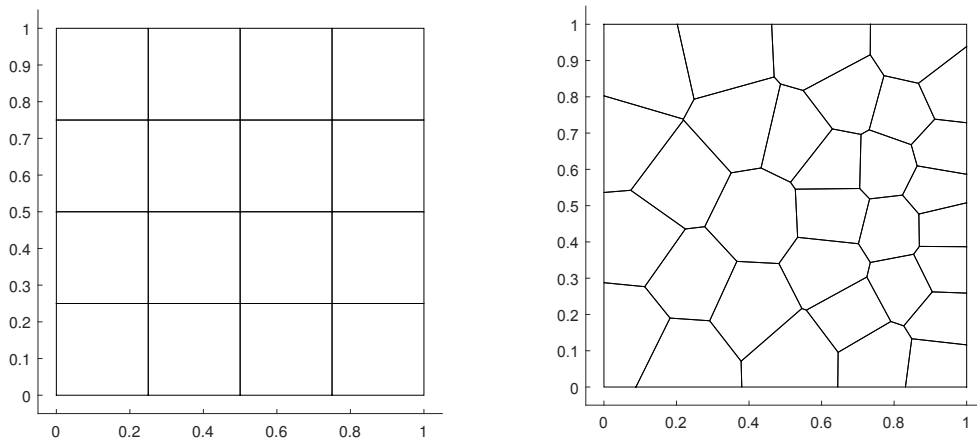


Figure 4: *Left:* Cartesian mesh. *Right:* Voronoi-Lloyd mesh.

In all the cases, we notice that the method becomes unstable after very few mesh refinements. This fact can be traced back to the computation of the Robin matrix \mathbf{R} in (31) and of the right-hand side vector \mathbf{f} in (33). Indeed, in both cases, we locally invert the edge plane wave mass matrices \mathbf{G}_0^e in (32) on all boundary edges $e \in \mathcal{E}_n^B$. Such matrices are highly ill-conditioned; see Figure 7, where the condition number of the matrix \mathbf{G}_0^e for the edge e with endpoints in $\mathbf{a} = [0, 0]$ and $\mathbf{b} = [0, h]$ is depicted in dependence of h for the set of directions $\{\mathbf{d}_\ell^{(0)}\}_{\ell=1}^p$ in (39) and for

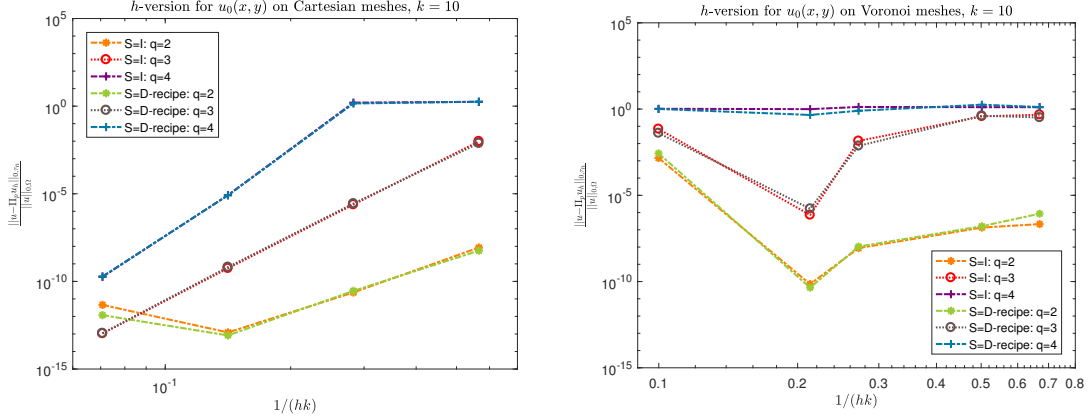


Figure 5: Approximate relative L^2 bulk errors for the h -version of the method for u_0 in (35) with $k = 10$, $q = 2, 3$, and 4, on Cartesian meshes (*left*) and Voronoi meshes (*right*) with directions $\{\mathbf{d}_\ell^{(0)}\}_{\ell=1}^p$ as in (39), and the identity and modified D-recipe stabilizations in (37) and (38), respectively.

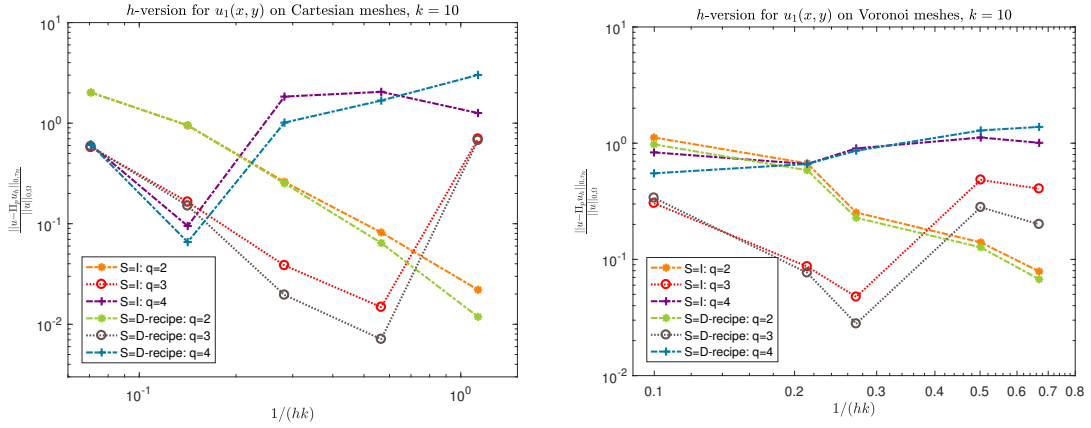


Figure 6: Approximate relative L^2 bulk errors for the h -version of the method for u_1 in (35) with $k = 10$, $q = 2, 3$, and 4, on Cartesian meshes (*left*) and Voronoi meshes (*right*) with directions $\{\mathbf{d}_\ell^{(0)}\}_{\ell=1}^p$ as in (39), and the identity and modified D-recipe stabilizations in (37) and (38), respectively.

different values of $q = 2, 3$, and 4. In particular, one can also observe that the ill-conditioning grows together with the effective plane wave degree q .

Rebus sic stantibus, the present version of the method is not reliable. For this reason, we propose in Section 5 a numerical recipe to mitigate this ill-conditioning.

5 The modified nonconforming Trefftz-VEM

As discussed in Section 4, the method (20) as constructed in Section 3 does not provide robust numerical performance. The aim of this section is to describe a recipe to damp the condition number of the local Trefftz-VE matrices and make the method reliable. In particular, in Section 5.1, we present a modification to the original method, whose implementation aspects are described in Section 5.2, and which is tested in Section 5.3. We deem that such a modification can be employed in other nonconforming settings.

5.1 A cure for the ill-conditioning

The main idea of the modification of the method is that, instead of applying the filtering process of Algorithm 1, we first compute, on each edge $e \in \mathcal{E}_n$, an eigendecomposition of the edge plane

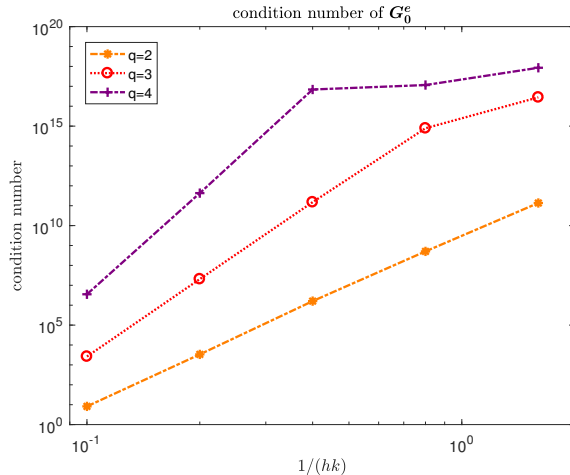


Figure 7: Condition number of \mathbf{G}_0^e defined in (32) for the edge e with endpoints in $\mathbf{a} = [0, 0]$ and $\mathbf{b} = [0, h]$ in terms of hk for the set of directions $\{\mathbf{d}_\ell^{(0)}\}_{\ell=1}^p$ in (39) and different values of $q = 2, 3,$ and 4 .

wave mass matrix \mathbf{G}_0^e :

$$\mathbf{G}_0^e \mathbf{Q}^e = \mathbf{Q}^e \mathbf{\Lambda}^e. \quad (40)$$

Here, $\mathbf{G}_0^e \in \mathbb{R}^{p \times p}$ is defined similarly as in (30), but using the traces of all bulk plane waves in $\mathbb{P}\mathbb{W}_p(K)$ and not those after filtering as in $\mathbb{P}\mathbb{W}_p^c(e)$, see (6). Therefore, \mathbf{G}_0^e can be singular (e.g. when two bulk plane waves have the same trace on e). Moreover, we do not longer require that the constants belong to the plane wave trace space. Note that the requirement that the constant functions are contained in the plane wave trace spaces was instrumental in the proof of the abstract error estimate in [37], but seems to be not necessary in practice.

In the decomposition (40), the matrices $\mathbf{Q}^e \in \mathbb{R}^{p \times p}$ and $\mathbf{\Lambda}^e \in \mathbb{R}^{p \times p}$ denote the eigenvector and eigenvalue matrices, respectively. Equivalently, the j -th column of \mathbf{Q}^e contains the coefficients of the expansion of the new orthonormal plane wave w_j^e with respect to the traces of the bulk plane waves w_ℓ^K , $\ell = 1, \dots, p$, on e .

Next, we determine the positions of the eigenvalues on the diagonal of the matrix $\mathbf{\Lambda}^e$ which are zero or “close” to zero (up to a given tolerance σ), and we remove the corresponding columns of \mathbf{Q}^e . Doing so, we end up with a set of filtered orthonormalized plane waves. Having this, all the VE matrices discussed in Section 3 are computed employing the new filtered basis.

We highlight that this new filtering process is highly significant in presence of small edges and when employing a large number of initial plane wave basis functions. Moreover, it does not affect the rate of convergence of the method, as we will see in the numerical experiments. Heuristically, this is not surprising since the traces of the removed plane waves “almost” (depending on the choice of σ) belong to the span of the traces of the remaining ones. A pseudo-code of this procedure is given in Algorithm 2.

Remark 3. We highlight that the influence of the choice of the parameter σ in Algorithm 2 on the convergence of the method will be discussed in Remark 5. Further, we note that, from a practical point of view, due to the presence of eigenvalues/singular values close to zero, the computation of an orthonormal basis in `Matlab` via the eigendecomposition in step 1(b) in Algorithm 2 seems to be more robust than other procedures, such as SVD.

Remark 4. The strategy presented in Algorithm 2 seems to be natural in the nonconforming setting. In fact, the basis functions are defined implicitly inside each elements by prescribing explicit conditions on the traces on each edge, and thus they can be modified edgewise without affecting their behavior on the other edges. This is not the case, for instance, in DG methods, where a modification of the basis functions implies a change in the behavior of such functions over *all* the edges.

Algorithm 2

Let $\sigma > 0$ be a given tolerance.

1. For all the edges $e \in \mathcal{E}_n$:

(a) Assemble the real-valued, symmetric, and possibly singular matrix $\mathbf{G}_0^e \in \mathbb{R}^{p \times p}$ given as in (32) by

$$(\mathbf{G}_0^e)_{j,\ell} = (w_\ell^e, w_j^e)_{0,e} \quad \forall j, \ell = 1, \dots, p. \quad (41)$$

(b) Starting from \mathbf{G}_0^e , compute the eigendecomposition (40):

$$\mathbf{G}_0^e \mathbf{Q}^e = \mathbf{Q}^e \mathbf{\Lambda}^e,$$

where $\mathbf{Q}^e \in \mathbb{R}^{p \times p}$ is a matrix whose columns are right-eigenvectors, and $\mathbf{\Lambda}^e \in \mathbb{R}^{p \times p}$ is a diagonal matrix containing the corresponding eigenvalues.

(c) Determine the eigenvalues with (absolute) value smaller than the tolerance σ and remove the columns of \mathbf{Q}^e corresponding to these eigenvalues. Denote the number of remaining columns of \mathbf{Q}^e by $\widehat{p}_e \leq p$. The remaining columns of \mathbf{Q}^e are relabelled by $1, \dots, \widehat{p}_e$.

(d) Define the new $L^2(e)$ orthonormal edge functions \widehat{w}_ℓ^e , $\ell = 1, \dots, \widehat{p}_e$, in terms of the old ones w_r^e , $r = 1, \dots, p$, as

$$\widehat{w}_\ell^e := \sum_{r=1}^p \mathbf{Q}_{r,\ell}^e w_r^e. \quad (42)$$

2. By using (42), build up the new local matrices $\widehat{\mathbf{G}}^K$, $\widehat{\mathbf{B}}^K$, and $\widehat{\mathbf{D}}^K$ for every element $K \in \mathcal{T}_n$, and assemble the global matrices $\widehat{\mathbf{A}}$, $\widehat{\mathbf{R}}$, and the global right-hand side vector $\widehat{\mathbf{f}}$.

5.2 Details on the implementation of the modified method

Here, we discuss some aspects of the implementation of the modified nonconforming Trefftz-VEM defined as in Algorithm 2.

Definition of the new degrees of freedom and canonical basis functions. Given $K \in \mathcal{T}_n$, let $\widehat{V}_h(K)$ be defined similarly as $V_h(K)$ in (7), where the only difference is that the space $\mathbb{P}\mathbb{W}_p^c(e)$ in (7) is replaced by $\mathbb{P}\mathbb{W}_p(K)|_e$. In addition, given $e \in \mathcal{E}_n$, let $\{\widehat{w}_\ell^e\}_{\ell=1}^{\widehat{p}_e}$ be the set of the new (L^2 orthonormal) edge functions determined with the Algorithm 2. The definitions of the global nonconforming Trefftz-VE spaces in (11) and (12), and of the L^2 projector in (14) are changed accordingly.

Using (42), we modify the degrees of freedom and the definition of the canonical basis functions as follows. The new local degrees of freedom $\{\widehat{\text{dof}}_{r,j}\}_{r=1, \dots, n_K, j=1, \dots, \widehat{p}_{e_r}}$ related to an element $K \in \mathcal{T}_n$ are given, for any $v_h \in \widehat{V}_h(K)$, as

$$\widehat{\text{dof}}_{r,j}(v_h) := \frac{1}{h_{e_r}} \int_{e_r} v_h \overline{\widehat{w}_j^{e_r}} ds \quad \forall j = 1, \dots, \widehat{p}_{e_r}. \quad (43)$$

Further, the set of the new local canonical basis functions $\{\widehat{\varphi}_{s,\ell}\}_{s=1, \dots, n_K, \ell=1, \dots, \widehat{p}_{e_s}}$ associated with the local set of degrees of freedom (43) is the set of functions in the space $\widehat{V}_h(K)$ with the property that

$$\widehat{\text{dof}}_{r,j}(\widehat{\varphi}_{s,\ell}) = \delta_{r,s} \delta_{j,\ell}, \quad \forall r, s = 1, \dots, n_K, \forall j = 1, \dots, \widehat{p}_{e_r}, \forall \ell = 1, \dots, \widehat{p}_{e_s}.$$

As usual, the sets of global degrees of freedom and of the canonical basis functions are obtained by coupling the local counterparts in a nonconforming fashion.

Next, we show how the new matrices $\widehat{\mathbf{G}}^K$, $\widehat{\mathbf{B}}^K$, $\widehat{\mathbf{D}}^K$, $\widehat{\mathbf{A}}$, and $\widehat{\mathbf{R}}$, and the new discrete right-hand side $\widehat{\mathbf{f}}$, counterparts of those described in Section 3, can be built starting from the original ones.

Computation of new local matrices.

- $\widehat{\mathbf{G}}^K$: This matrix coincides with \mathbf{G}^K since it is computed via plane waves in the bulk.
- $\widehat{\mathbf{B}}^K$: For all $j = 1, \dots, p$, $s = 1, \dots, n_K$, $\ell = 1, \dots, \widehat{p}_{e_s}$, it holds

$$(\widehat{\mathbf{B}}^K)_{j,(s,\ell)} := a^K(\widehat{\varphi}_{s,\ell}, w_j^K) = -ik(\mathbf{d}_j \cdot \mathbf{n}_{K|_{e_s}}) e^{-ik\mathbf{d}_j \cdot (\mathbf{x}_{e_s} - \mathbf{x}_K)} \int_{e_s} \widehat{\varphi}_{s,\ell} \overline{e^{ik\mathbf{d}_j \cdot (\mathbf{x} - \mathbf{x}_{e_s})}} ds. \quad (44)$$

Expressing the old edge function $w_j^{e_s}$ in terms of the novel ones

$$w_j^{e_s} = \sum_{\zeta=1}^{\widehat{p}_{e_s}} (\mathbf{Q}^e)_{\zeta,j}^T \widehat{w}_\zeta^{e_s}, \quad (45)$$

and plugging this into (44) lead to

$$(\widehat{\mathbf{B}}^K)_{j,(s,\ell)} = -ik \overline{(\mathbf{Q}^e)_{\ell,j}^T} (\mathbf{d}_j \cdot \mathbf{n}_{K|_{e_s}}) e^{-ik\mathbf{d}_j \cdot (\mathbf{x}_{e_s} - \mathbf{x}_K)} h_{e_s}.$$

- $\widehat{\mathbf{D}}^K$: Given $r \in \mathcal{M}_K$, $j = 1, \dots, \widehat{p}_{e_r}$, $\ell = 1, \dots, p$, a direct computation based again on the expansion (45) gives

$$(\widehat{\mathbf{D}}^K)_{(r,j),\ell} := \widehat{\text{dof}}_{r,j}(w_\ell^K) = \frac{1}{h_{e_r}} \int_{e_r} w_\ell^K \overline{\widehat{w}_j^{e_r}} ds = \sum_{\zeta=1}^p \overline{\mathbf{Q}_{\zeta,j}^e} \frac{1}{h_{e_r}} \int_{e_r} w_\ell^K \overline{w_\zeta^{e_r}} ds.$$

- $\widehat{\mathbf{A}}$: Starting from the local matrices

$$\widehat{\mathbf{A}}^K = \overline{\widehat{\mathbf{B}}^K}^T \overline{\widehat{\mathbf{G}}^K}^{-T} \widehat{\mathbf{B}}^K + (\widehat{\mathbf{I}}^K - \widehat{\mathbf{\Pi}}^K)^T \widehat{\mathbf{S}}^K (\widehat{\mathbf{I}}^K - \widehat{\mathbf{\Pi}}^K),$$

see (26), $\widehat{\mathbf{A}}$ is assembled as in (23), where $\widehat{\mathbf{\Pi}}^K$ is defined similarly as in (25).

- $\widehat{\mathbf{R}}$: We need to compute

$$\widehat{\mathbf{R}}_{(\tilde{r},\tilde{j}),(\tilde{s},\tilde{\ell})} = ik\theta \sum_{e \in \mathcal{E}_n^R} \int_e (\Pi_p^{0,e} \widehat{\varphi}_{\tilde{s},\tilde{\ell}}) \overline{(\Pi_p^{0,e} \widehat{\varphi}_{\tilde{r},\tilde{j}})} ds$$

$$\forall \tilde{r}, \tilde{s} = 1, \dots, N_e, \forall \tilde{j} = 1, \dots, \widehat{p}_{e_{\tilde{r}}}, \forall \tilde{\ell} = 1, \dots, \widehat{p}_{e_{\tilde{s}}}.$$

Given $e \in \mathcal{E}_n^R$, we only describe here the assembly of the matrix $\widehat{\mathbf{R}}^e \in \mathbb{C}^{p_e \times p_e}$, which takes into account the local contributions of the basis functions associated with e . Then, $\widehat{\mathbf{R}}$ is assembled as in (29). Given z the local index of e , for every $j, \ell = 1, \dots, \widehat{p}_e$, it holds

$$(\widehat{\mathbf{R}}^e)_{\ell,j} = \int_e (\Pi_p^{0,e} \widehat{\varphi}_{z,j}) \overline{(\Pi_p^{0,e} \widehat{\varphi}_{z,\ell})} ds. \quad (46)$$

By writing each $\Pi_p^{0,e} \widehat{\varphi}_{z,j}$, $j = 1, \dots, \widehat{p}_e$, as a linear combination of the $L^2(e)$ orthonormal plane waves \widehat{w}_θ^e , $\theta = 1, \dots, \widehat{p}_e$, and inserting this into (46), one obtains

$$\widehat{\mathbf{R}}^e = \overline{(\widehat{\mathbf{B}}_0^e)^T} \overline{(\widehat{\mathbf{G}}_0^e)^{-T}} \widehat{\mathbf{B}}_0^e,$$

where

$$(\widehat{\mathbf{B}}_0^e)_{j,\ell} = (\widehat{\varphi}_{z,\ell}, \widehat{w}_j^e)_{0,e} = h_e \delta_{j,\ell} \quad \forall j, \ell = 1, \dots, \widehat{p}_e,$$

and

$$(\widehat{\mathbf{G}}_0^e)_{j,\ell} = (\widehat{w}_\ell^e, \widehat{w}_j^e)_{0,e} = \sum_{\zeta,\eta=1}^{\widehat{p}_e} \mathbf{Q}_{\eta,\ell}^e \overline{\mathbf{Q}_{\zeta,j}^e} \int_e w_\eta^e \overline{w_\zeta^e} ds,$$

which can be represented as

$$\widehat{\mathbf{G}}_0^e = \overline{(\mathbf{Q}^e)^T} \mathbf{G}_0^e \mathbf{Q}^e$$

with \mathbf{G}_0^e given in (41).

- $\widehat{\mathbf{f}} := \widehat{\mathbf{f}}^N + \widehat{\mathbf{f}}^R$: We restrict here ourselves to the computation of $\widehat{\mathbf{f}}^N$, which is given by

$$(\widehat{\mathbf{f}}^N)_{(\tilde{r}, \tilde{j})} = \sum_{e \in \mathcal{E}_n^N} \int_e g_N(\overline{\Pi_p^{0,e} \widehat{\varphi}_{\tilde{r}, \tilde{j}}}) \quad \forall \tilde{r} = 1, \dots, N_e, \forall \tilde{j} = 1, \dots, \widehat{p}_{e_{\tilde{r}}}.$$

The local vector $\widehat{\mathbf{f}}^{N,e} \in \mathbb{C}^{p_e}$ for a given $e \in \mathcal{E}_n^N$, with z denoting again the local index associated with e , has the form

$$(\widehat{\mathbf{f}}^{N,e})_\ell = \int_e g_N(\overline{\Pi_p^{0,e} \widehat{\varphi}_{z,\ell}}) ds = \sum_{\eta=1}^{\widehat{p}_e} \widehat{\beta}_\eta^{(\ell)} \int_e g_N \overline{\widehat{w}_\eta^e} ds = \sum_{\eta=1}^{\widehat{p}_e} \sum_{\zeta=1}^p \widehat{\beta}_\eta^{(\ell)} (\mathbf{Q}^e)_{\zeta,\eta} \int_e g_N \overline{w_\zeta^e} ds.$$

- The Dirichlet boundary conditions are incorporated in the global system of linear equations as already shown in Section 3.5, by requiring that

$$\int_{e_\zeta} (u_h - g_D) \overline{\widehat{w}_j^{e_\zeta}} ds = 0 \quad \forall j = 1, \dots, \widehat{p}_{e_\zeta}, \forall e_\zeta \in \mathcal{E}_n^D,$$

which leads to

$$u_{\zeta,j} = \frac{1}{h_{e_\zeta}} \int_{e_\zeta} g_D \overline{\widehat{w}_j^{e_\zeta}} ds = \frac{1}{h_{e_\zeta}} \sum_{r=1}^p \overline{(\mathbf{Q}_{r,j}^{e_\zeta})} \int_{e_\zeta} g_D \overline{w_r^{e_\zeta}} ds \quad \forall j = 1, \dots, \widehat{p}_{e_\zeta}, \forall e_\zeta \in \mathcal{E}_n^D.$$

5.3 Numerical results with the modified method

In this section, we discuss the h -, p -, and hp -versions of the modified method and assess the improvements in the numerical performance. We will see that the modified method is not only better conditioned, but also the number of degrees of freedom needed to achieve a given accuracy of the numerical approximation is significantly lower than in the original version in Section 3. Moreover, we compare the modified nonconforming Trefftz-VEM with the PWVEM of [40] and with the more established PWDG method [37].

In all the numerical tests throughout this paper, the tolerance σ in Algorithm 2 is set to 10^{-13} . Other choices and their influence on the method are discussed in Remark 5.

Additionally to the boundary value problems (3) on $\Omega := (0, 1)^2$ with known solutions u_0 and u_1 in (35), we consider boundary value problems for $\theta = 1$ and $\Gamma_R = \partial\Omega$ with exact solutions

$$\begin{aligned} u_2(x, y) &:= H_0^{(1)}(k|\mathbf{x} - \mathbf{x}_0|), \quad \mathbf{x}_0 = (-0.25, 0), \\ u_3(x, y) &:= J_\xi(kr) \cos(\xi\theta), \quad \xi = \frac{2}{3}, \end{aligned} \tag{47}$$

where $H_0^{(1)}$ is the zeroth-order Hankel functions of the first kind, J_ξ denotes the Bessel function of the first kind, and r and θ are the polar coordinates of $(x, y - 0.5)$, see [1, Chapters 9 and 10]. Note that the function u_2 is analytic over Ω , but u_3 has a singularity at $(0, 0.5)$; more precisely, $u_3 \in H^{\xi+1-\epsilon}(\Omega)$ for all $\epsilon > 0$ arbitrarily small, but $u_3 \notin H^{\xi+1}(\Omega)$. The contour plots of the real parts for the two test cases in (47) with $k = 20$ are plotted in Figure 8.

We also consider the test of a scattering problem in Section 5.3.1.1 (here, $\Gamma_R \neq \partial\Omega$).

5.3.1 h -version

We first show the modified method on the *patch test* u_0 defined in (35) to check the consistency (16) and to validate the gain in robustness with respect to the original version, cf. Section 4. Let $\{\mathbf{d}_\ell^{(0)}\}_{\ell=1}^p$ be the set of directions given in (39). The numerical experiments are again performed on sequences of quasi-uniform Cartesian meshes and Voronoi-Lloyd meshes, see Figure 4, for $k = 10$ and 20, and effective plane wave degree $q = 4$ and 7. Recall that the number of used bulk plane waves is $p = 2q + 1$. Further, we employ the *modified D -recipe stabilization* in (38). In Figure 9, the approximate relative H^1 bulk errors in (36) are plotted. We observe that the patch test is fulfilled for meshes with a moderately small mesh size. The plots indicate that the modified version

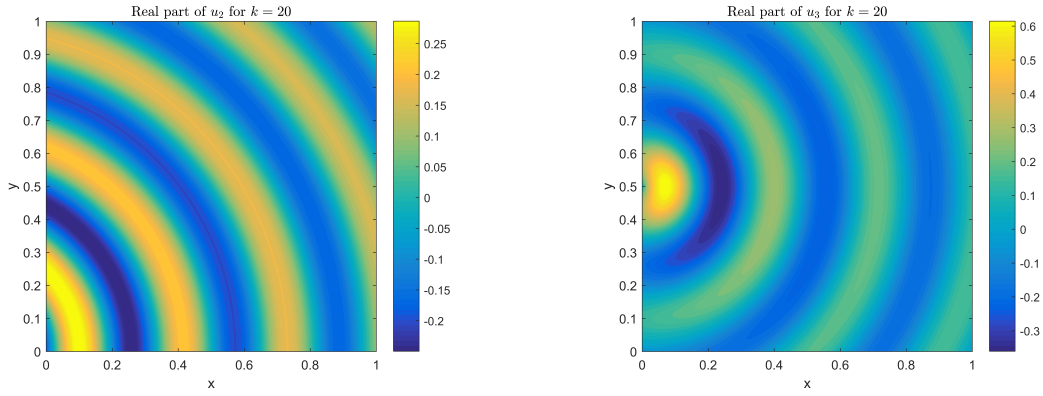


Figure 8: Real parts of the functions u_2 (left) and u_3 (right) defined in (47) for $k = 20$.

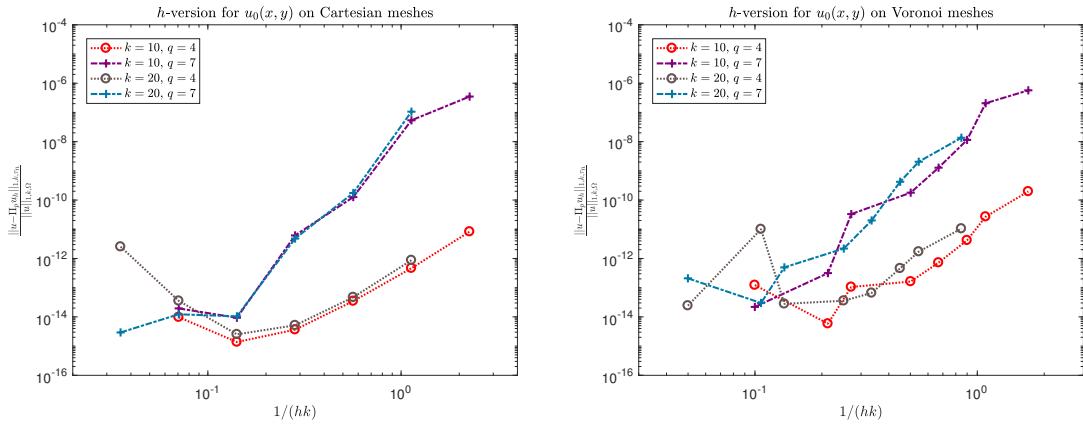


Figure 9: h -version of the method for u_0 in (35) with $k = 10$ and 20 , and $q = 4$ and 7 , with the sets of directions $\{\mathbf{d}_\ell^{(0)}\}_{\ell=1}^p$ as in (39) and the modified D-recipe stabilization (38) on Cartesian meshes (left) and Voronoi meshes (right).

is much more stable than the original one, see Figure 5. Nevertheless, also this modified version is affected by ill-conditioning, which results in the increase of the errors for decreasing mesh size h , as typical of plane wave-based methods.

As a second test, we investigate the h -version for the exact solution u_1 in (35) with $k = 10$, 20 , and 40 , and $q = 4$ and 7 , employing the same choice of directions, meshes, and stabilizations as before. The numerical results are depicted for the Cartesian meshes in Figure 10 and Table 1 ($k = 20$, $q = 7$), and for the Voronoi meshes in Figure 11 and Table 2 ($k = 20$, $q = 7$). In all cases the errors were computed accordingly with (36). In Table 1 and 2 we further compare the number of degrees of freedom using the modified version of the method with the original one. The reduction of degrees of freedom in % is presented in the last column.

Here, we mention that the tests with exact solution u_2 give similar results to those for the smooth solution u_1 and are postponed to Sections 5.3.4 and 5.3.5, where the modified nonconforming Trefftz-VEM will be compared with the PWVEM [40] and the PWDG [27], respectively.

h	N_{dof}	rel. H^1 error	rate	rel. L^2 error	rate	N_{dof} orig.	red. (%)
1.414e+00	46	4.6885e-01	—	4.7153e-01	—	48	4.17
7.071e-01	120	1.3527e-01	1.793	1.3185e-01	1.838	144	16.67
3.535e-01	340	1.0540e-03	7.004	5.4861e-04	7.909	480	29.17
1.767e-01	1008	6.1594e-06	7.419	1.4439e-06	8.570	1728	41.67
8.838e-02	3264	4.2394e-08	7.183	4.4716e-09	8.335	6528	50.00
4.419e-02	10560	1.6544e-07	-1.964	7.3453e-08	-4.038	25344	58.33

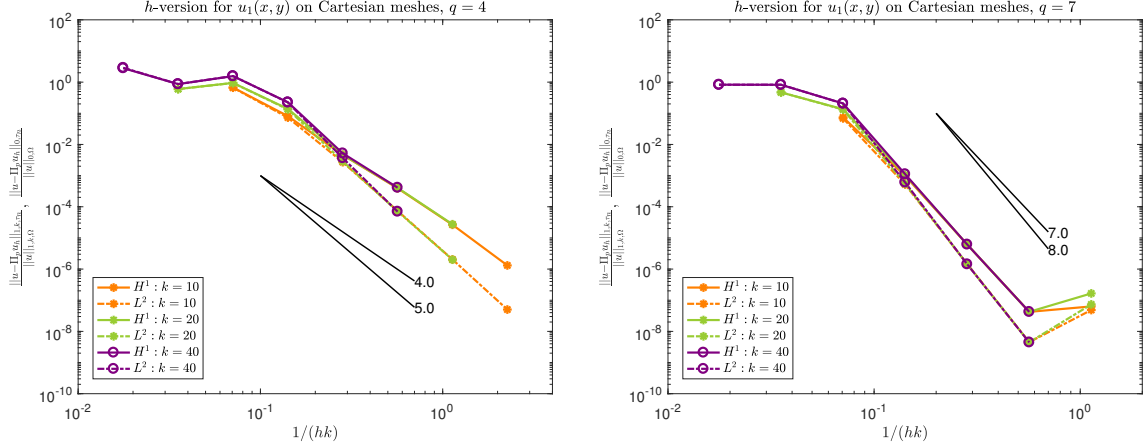


Figure 10: h -version of the modified method for u_1 in (35) with $k = 10, 20$, and 40 , and $q = 4$ (left) and 7 (right), with the sets of directions $\{\mathbf{d}_\ell^{(0)}\}_{\ell=1}^p$ as in (39) and the modified D-recipe stabilization (38) on Cartesian meshes.

Table 1: Relative errors for u_1 in (35) with $k = 20$, $q = 7$, and the directions $\{\mathbf{d}_\ell^{(0)}\}_{\ell=1}^p$ as in (39) on Cartesian meshes employing the modified method with the modified D-recipe stabilization (38).

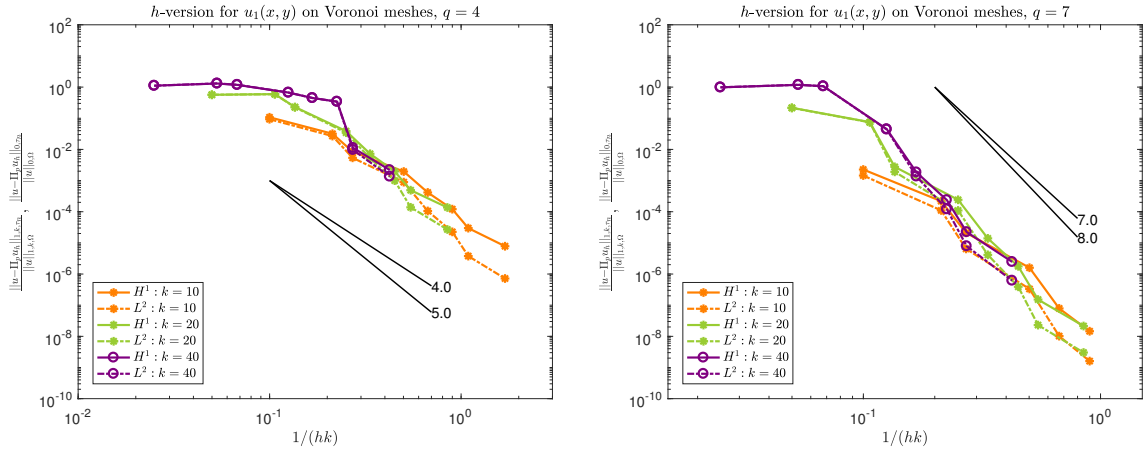


Figure 11: h -version of the modified method for u_1 in (35) with $k = 10, 20$, and 40 , and $q = 4$ (left) and 7 (right), with the sets of directions $\{\mathbf{d}_\ell^{(0)}\}_{\ell=1}^p$ as in (39) and the modified D-recipe stabilization (38) on Voronoi meshes.

h	N_{dof}	rel. H^1 error	rel. L^2 error	N_{dof} orig.	red. (%)
1.001e+00	131	2.1704e-01	2.1440e-01	182	28.02
4.697e-01	224	7.5289e-02	7.4015e-02	359	37.60
3.688e-01	394	2.7605e-03	1.9061e-03	713	44.74
1.993e-01	695	2.4147e-04	1.0970e-04	1477	52.95
1.493e-01	1243	1.3955e-05	4.1303e-06	2960	58.01
1.111e-01	2206	1.7662e-06	3.9013e-07	5998	63.22
9.171e-02	4002	1.5165e-07	2.3002e-08	12092	66.90
5.896e-02	7282	2.1462e-08	3.0271e-09	24304	70.04

Table 2: Relative errors for u_1 in (35) with $k = 20$, $q = 7$, and the directions $\{\mathbf{d}_\ell^{(0)}\}_{\ell=1}^p$ as in (39) on Voronoi meshes employing the modified method with the modified D-recipe stabilization (38).

We observe from Figures 10 and 11, and Tables 1 and 2 that the approximate relative H^1 and L^2 discretization errors in (36) of the method approximately converge with rate 4 and 5 for $q = 4$,

and 7 and 8 for $q = 7$, respectively. This is in agreement with the error estimate derived in [37], which established, for $h \rightarrow 0$ and analytic solutions, convergence rates of order q and $q + 1$, for the relative H^1 and L^2 errors, respectively. Note that due to the fact that the Voronoi meshes are not nested, the slopes indicating the convergence order are not as straight as in the Cartesian case.

In addition, we notice that the number of degrees of freedom was reduced significantly by making use of the orthonormalization process described in Algorithm 2 in comparison to the original version of the method, which employs the standard filtering process in Algorithm 1.

Next, we employ the *identity stabilization* (37) and compare the performance with the modified D-recipe stabilization for u_1 using the same meshes and parameters as above. The results for the relative H^1 errors in (36) are shown in Table 3.

Cartesian				Voronoi			
h	N_{dof}	D-recipe	identity	h	N_{dof}	D-recipe	identity
1.414e+00	46	4.6885e-01	4.8651e-01	1.001e+00	131	2.1704e-01	2.3510e-01
7.071e-01	120	1.3527e-01	2.0525e-01	4.697e-01	224	7.5289e-02	9.3167e-02
3.535e-01	340	1.0540e-03	2.4615e-02	3.688e-01	394	2.7605e-03	2.4375e-02
1.767e-01	1008	6.1594e-06	1.7224e-03	1.993e-01	695	2.4147e-04	8.5729e-03
8.838e-02	3264	4.2394e-08	1.2786e-05	1.493e-01	1243	1.3955e-05	2.4687e-03
4.419e-02	10560	1.6544e-07	6.4752e-07	1.111e-01	2206	1.7662e-06	6.0640e-04

Table 3: Relative H^1 errors for u_1 in (35) with $k = 20$, $q = 7$, and the directions $\{\mathbf{d}_\ell^{(0)}\}_{\ell=1}^p$ as in (39) on Cartesian (*left*) and Voronoi (*right*) meshes employing the modified method with the D-recipe stabilization (38) and the identity stabilization (37).

Compared to the modified D-recipe stabilization, the method based on the identity stabilization behaves worse. Similar results are obtained for the relative L^2 errors in (36). This fact highlights that picking a “good” stabilization is an important issue in the design of VEM [11, 21, 35].

Thus, in the sequel, we will always consider the modified nonconforming Trefftz-VEM endowed with the modified D-recipe stabilization (38).

As a last test in this section, we study the h -version of the method for the non-analytic solution u_3 in (47). Once again we perform the tests on the Cartesian meshes with $k = 10, 20$, and 40 , and $q = 4$ and 7 , in Figure 12. We point out that similar results were obtained employing Voronoi meshes.

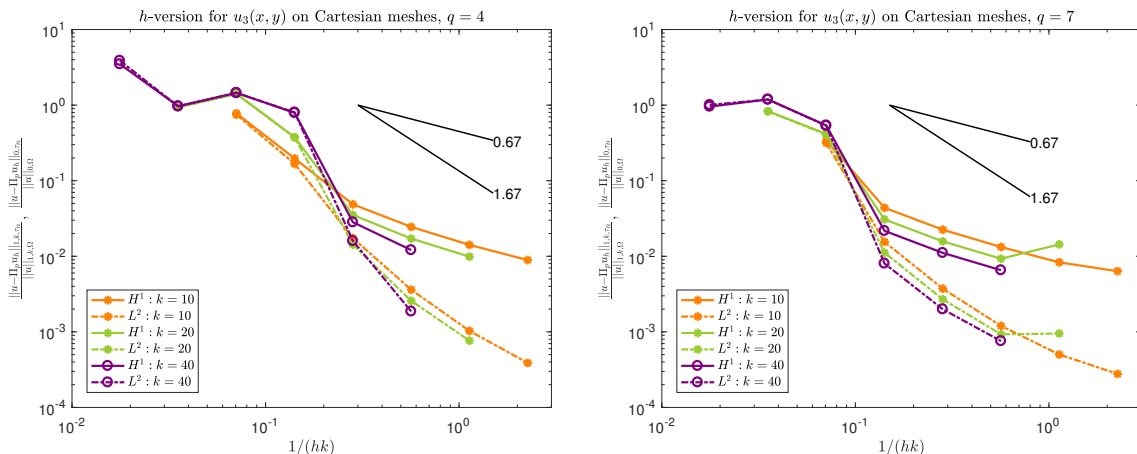


Figure 12: h -version of the method for u_3 in (35) with $k = 10, 20$, and 40 , and $q = 4$ (*left*) and 7 (*right*), with the sets of directions $\{\mathbf{d}_\ell^{(0)}\}_{\ell=1}^p$ as in (39) and the modified D-recipe stabilization (38) on Cartesian meshes.

The observed convergence rate for the approximate H^1 bulk error in (36) is $\frac{2}{3}$ and that for the approximate L^2 bulk error is $\frac{5}{3}$. This corresponds to the expected convergence rates $\min\{s, q\}$ and $\min\{s, q\} + 1$ for the H^1 and L^2 errors, respectively, where s is the regularity of the solution and q is the effective plane wave degree, see [37].

Remark 5. Here, we discuss and motivate the choice for the parameter σ in Algorithm 2, which so far has been set to 10^{-13} . In principle, it would have been more natural to take $\sigma = 10$ eps, where eps denotes the machine epsilon. With this choice, it would be basically guaranteed that the span of the filtered orthonormalized edge plane wave functions coincides with the non-orthonormalized edge plane wave space, up to a negligible difference. However, we could observe from numerical experiments that with smaller choices of σ , such as 10^{-13} , it is possible to achieve the same accuracy as when employing $\sigma = 10$ eps, but with less degrees of freedom, see Table 4, where we tested the h -version of the modified nonconforming Trefftz-VEM with analytical solution u_2 in (47) on a sequence of Voronoi-Lloyd meshes of the type in Figure 4 (right) for the two above-mentioned choices of σ with $k = 10$ and $q = 7$.

h	$\sigma = 10$ eps		$\sigma = 10^{-13}$	
	N_{dof}	rel. L^2 error	N_{dof}	rel. L^2 error
1.001346e+00	113	6.174135e-03	106	6.147714e-03
4.697545e-01	201	4.285982e-04	189	4.337061e-04
3.688297e-01	353	6.529610e-05	327	6.250524e-05
1.993180e-01	631	6.754430e-06	578	6.625276e-06
1.493758e-01	1139	1.572124e-07	1037	1.512503e-07
1.111597e-01	2053	6.369678e-08	1886	6.294611e-08
9.171171e-02	3745	2.514794e-08	3445	2.441118e-08

Table 4: h -version of the modified method for the analytical solution u_2 in (47), $k = 10$, $q = 7$, on Voronoi-Lloyd meshes of the type in Figure 4 with different choices of σ in Algorithm 2. The relative L^2 errors are computed accordingly with (36).

5.3.1.1 Application to an acoustic scattering problem. In this section, we consider the scattering of acoustic waves at a scatterer $\Omega_{Sc} \subset \mathbb{R}^2$ with polygonal boundary Γ_{Sc} . We study the cases of a sound-soft and sound-hard scatterers. The total field $u = u^S + u^I$, u^S and u^I denoting the scattered and the incident fields, respectively, satisfies

$$(i) \begin{cases} -\Delta u - k^2 u = 0 & \text{in } \Omega_{Sc}^c \\ u = 0 & \text{on } \Gamma_{Sc}, \end{cases} \quad (ii) \begin{cases} -\Delta u - k^2 u = 0 & \text{in } \Omega_{Sc}^c \\ \nabla u \cdot \mathbf{n}_\Omega = 0 & \text{on } \Gamma_{Sc}, \end{cases}$$

respectively, where $\Omega_{Sc}^c := \mathbb{R}^2 \setminus \overline{\Omega_{Sc}}$, and both problems are endowed with the Sommerfeld radiation condition at infinity:

$$\lim_{|\mathbf{x}| \rightarrow \infty} |\mathbf{x}| \left(\frac{\partial u^S(\mathbf{x})}{\partial |\mathbf{x}|} + iku^S(\mathbf{x}) \right) = 0, \quad (48)$$

see [19, Sect. 2.1].

By truncating the unbounded domain Ω_{Sc}^c and approximating the Sommerfeld radiation condition (48) by a first order absorbing impedance condition on the artificial boundary, one obtains

$$(iii) \begin{cases} -\Delta u - k^2 u = 0 & \text{in } \Omega \\ u = 0 & \text{on } \Gamma_{Sc} \\ \nabla u \cdot \mathbf{n}_\Omega + iku = g_R & \text{on } \Gamma_R, \end{cases} \quad (iv) \begin{cases} -\Delta u - k^2 u = 0 & \text{in } \Omega \\ \nabla u \cdot \mathbf{n}_\Omega = 0 & \text{on } \Gamma_{Sc} \\ \nabla u \cdot \mathbf{n}_\Omega + iku = g_R & \text{on } \Gamma_R, \end{cases} \quad (49)$$

where $\Omega := \Omega_R \setminus \overline{\Omega_{Sc}}$, with Ω_R denoting the truncated domain with boundary Γ_R , and $g_R = \nabla u^I \cdot \mathbf{n}_\Omega + ik\theta u^I$ is the impedance trace of the incoming wave. Both problems (iii) and (iv) in (49) are well-posed, according to Theorem 2.1. Note that in the context of acoustic scattering, the unknown function u in (49) represents the acoustic pressure, rather than the displacement.

For the numerical tests, we fix $\Omega = (-1, 2) \times (0, 3) \setminus [0, 1] \times [1, 2]$ and employ uniform Cartesian meshes, see Figure 13.

As incident fields, we consider the plane wave functions u_0 and u_1 in (35), as well as the plane wave given by

$$u_4(x, y) := \exp \left(ik \left(\cos \left(\frac{2\pi}{17} \right) x + \sin \left(\frac{2\pi}{17} \right) y \right) \right). \quad (50)$$

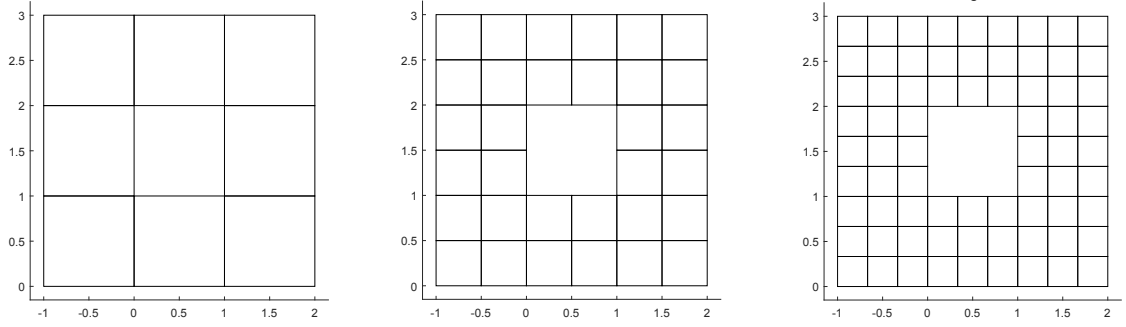


Figure 13: First three Cartesian meshes in the decomposition over the domain $\Omega = (-1, 2) \times (0, 3) \setminus [0, 1] \times [1, 2]$.

In Figures 14 and 15, the real parts of the computed total fields for the sound-hard and sound-soft cases, respectively, are plotted for the different incident fields with $k = 15$. As effective plane wave degree we choose $q = 10$ (namely $p = 21$ bulk plane waves).

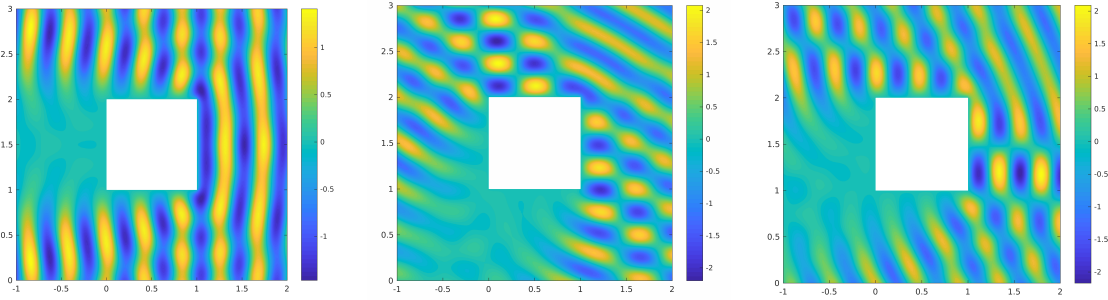


Figure 14: Real parts of the total fields for the sound-soft scattering employing as incident field the plane waves given by u_0 (left) and u_1 (center) in (35), and u_4 (right) in (50), with $k = 15$.

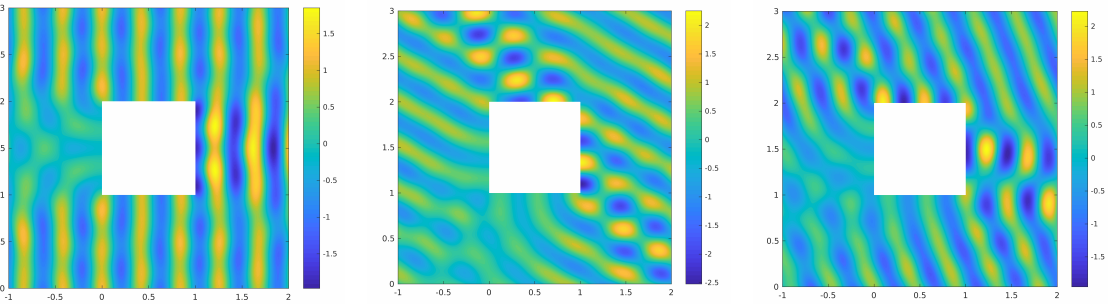


Figure 15: Real parts of the total fields for the sound-hard scattering employing as incident field the plane waves given by u_0 (left) and u_1 (center) in (35), and u_4 (right) in (50), with $k = 15$.

The relative errors are computed accordingly with (36), where, since an exact solution u is not known in closed form, u was chosen to be the discrete solution on a very fine mesh. In Figure 16, the obtained results are plotted. In both cases, the convergence rates are approximately 1.5 and 2.1 for the relative H^1 and L^2 errors, respectively.

5.3.2 p -version

We test numerically the p -version of the modified nonconforming Trefftz-VEM, that is, we achieve convergence by keeping fixed a mesh and increasing the local effective degree. To this end, we

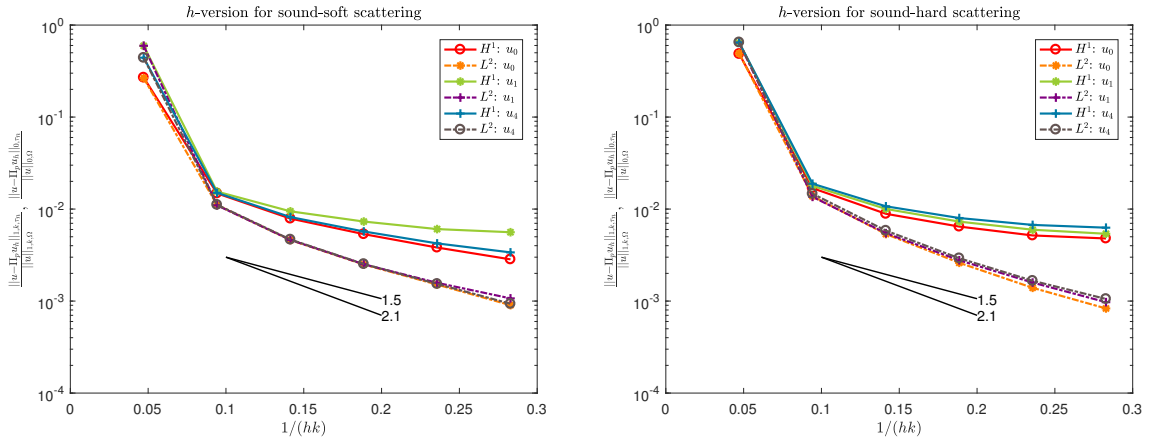


Figure 16: h -version of the modified method for the scattering problems (49) with $k = 15$ and $q = 10$. *Left:* sound-soft scattering; *right:* sound-hard scattering. The relative errors are computed accordingly with (36).

consider the two meshes shown in Figure 17. Each of them consists of eight elements. The first one is a Voronoi-Lloyd mesh, and the second is a mesh whose elements are not star-shaped with respect to any ball. In the sequel, we will refer to these meshes as mesh (a) and mesh (b), respectively.

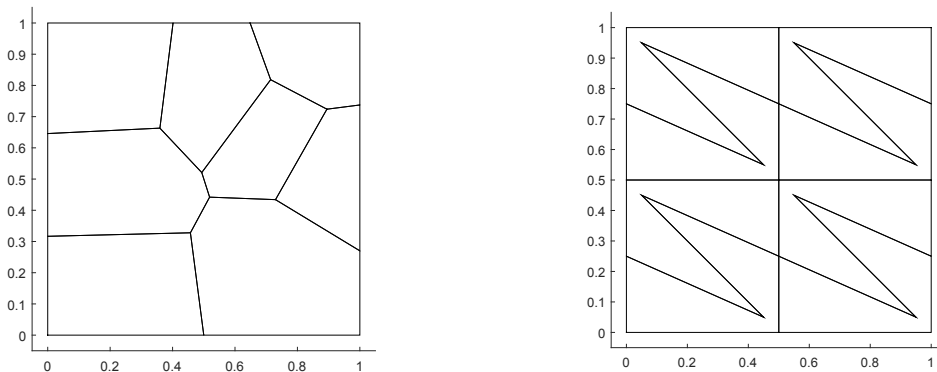


Figure 17: Different types of meshes made of eight elements; *left:* mesh (a), *right:* mesh (b).

To start with, we first investigate the p -version of the modified method for the test case with analytical solution u_1 in (35), employing different values of $k = 10, 20$, and 40 . The obtained numerical results are shown in Figure 18.

Also in this case, the tests with analytical solution u_2 in (47) lead to similar results and are postponed to the forthcoming Section 5.3.4, where the results are compared with the PWVEM and the PWDG.

For both meshes, we observe that after a pre-asymptotic regime, the modified method is able to reach exponential convergence in terms of the effective degree q , before instability takes place, caused by the haunting ill-conditioning of the plane wave basis. The pre-asymptotic regime is much wider for higher wave numbers, which is typical of plane wave-based methods. We underline that, despite the p -version of the nonconforming Trefftz-VEM has not been investigated theoretically yet, the exponential decay of the error for analytic solutions is not surprising, cf. [9, 29, 43].

Next, we perform the same experiments on the non-analytic exact solution u_3 in (47). The corresponding plots are depicted in Figure 19. We notice that the convergence rate is not exponential any more, but rather algebraic. This is also an expected behavior of the p -version [9, 29, 43].

5.3.3 hp -version

We numerically investigate the hp -version of the modified nonconforming Trefftz-VEM.

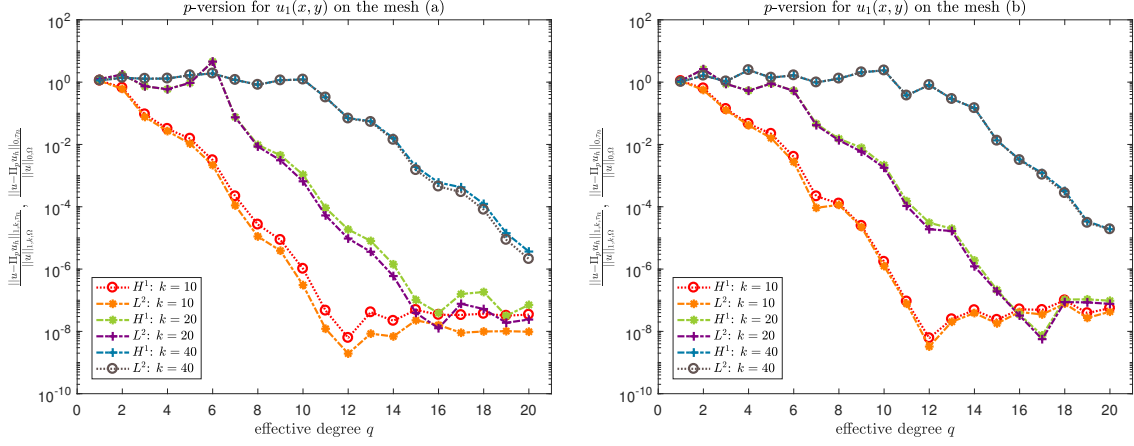


Figure 18: p -version of the modified method for u_1 in (35) on mesh (a) and (b) in Figure 17, from left to right.

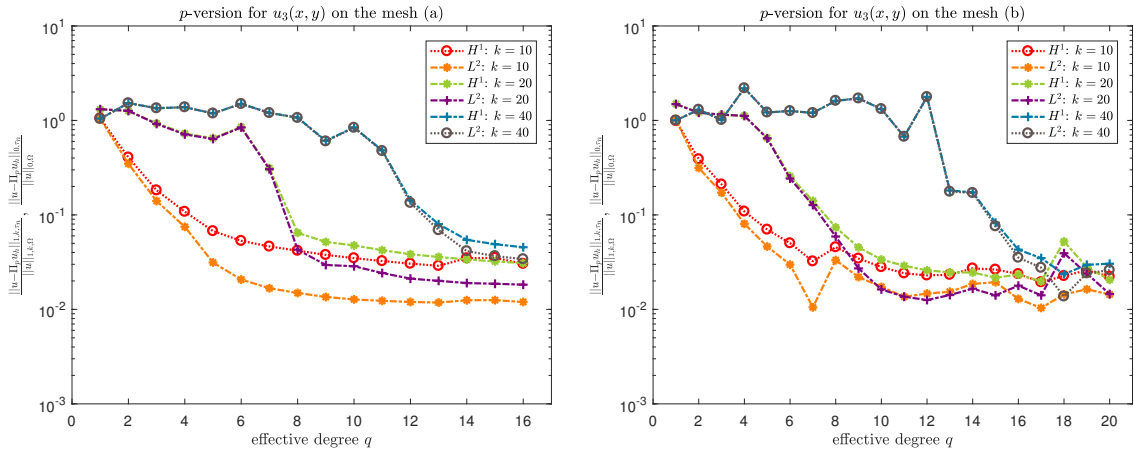


Figure 19: p -version of the modified method for u_3 in (47) on mesh (a) and (b) in Figure 17, from left to right.

By combining an h -refinement near solution singularities with a p -refinement in the elements where the solution is sufficiently smooth, exponential convergence of the errors in terms of a proper root of the number of degrees of freedom is expected. In the framework of Trefftz methods for the Helmholtz equation, a full hp -analysis was investigated for the PWDG method [30], where exponential convergence in terms of the square root of the number of degrees of freedom was proven.

Here, we build approximation spaces with variable number of plane wave directions element by element following the hp approach for the Poisson problem introduced in [10]. To this end, also taking into account that one has to impose continuity elementwise in the nonconforming sense (10), we proceed as follows.

Let us assume that we aim at approximating the solution u_3 defined in (47) on the square domain $\Omega = (0, 1)^2$; such function has a singularity at $\nu = (0, 0.5)$. We build a sequence of nested meshes that are refined towards ν . More precisely, we set $\tau_0 = \{\Omega\}$. Next, for $n \in \mathbb{N}$, the mesh \mathcal{T}_n is a polygonal mesh consisting of $n + 1$ layers, where the 0-th layer $L_{0,n}$ is the set of polygons abutting the singularity ν , whereas the ℓ -th layer is defined by induction as

$$L_{\ell,n} = \{K \in \mathcal{T}_n : \overline{K} \cap \overline{K_{\ell-1}} \neq \emptyset \text{ for some } K_{\ell-1} \in L_{\ell-1,n}, K \not\subset \cup_{j=0}^{\ell-1} L_j\}.$$

In order to achieve exponential convergence, one typically needs graded meshes towards ν . Hence, we require that the mesh size function h_K , for all elements $K \in \mathcal{T}_n$, satisfies

$$h_K \approx \begin{cases} \mu^n & \text{if } K \in L_{0,n}, \\ \frac{1-\mu}{\mu} \text{dist}(K, \nu) & \text{otherwise,} \end{cases} \quad (51)$$

where $\mu \in (0, 1)$ is referred to as the *grading parameter*. Moreover, we increase the dimension of the local spaces as follows. We associate with each $K \in \mathcal{T}_n$ a number q_K , defined as

$$q_K = \ell + 1 \quad \text{if } K \in L_{\ell,n}, \ell = 0, \dots, n-1, \quad (52)$$

and we build the local spaces $V_h(K)$ in (7) by using Dirichlet/impedance traces that are edgewise in $\widetilde{\mathbb{P}\mathbb{W}}_p^c(e)$, where the space $\widetilde{\mathbb{P}\mathbb{W}}_p^c(e)$ is defined as follows.

Given $q_{max,n} = \max_{K \in \mathcal{T}_n} q_K$, we first consider the set of $p_{max,n} := 2q_{max,n} + 1$ equidistributed directions $\{\tilde{\mathbf{d}}_{\ell,n}\}_{\ell=1}^{p_{max,n}}$. On each element K , we pick a set of $2q_K + 1$ directions obtained by removing $2(q_{max,n} - q_K)$ selected directions from the original set. Thus, elements abutting the singularity will have a small number of directions, which then increases linearly with the index of the layer.

In order to select such directions to be removed, we order the set $\{\tilde{\mathbf{d}}_{\ell,n}\}_{\ell=1}^{p_{max,n}}$ by picking first the directions with increasing odd indices and next those with even ones, see Figure 20. At this

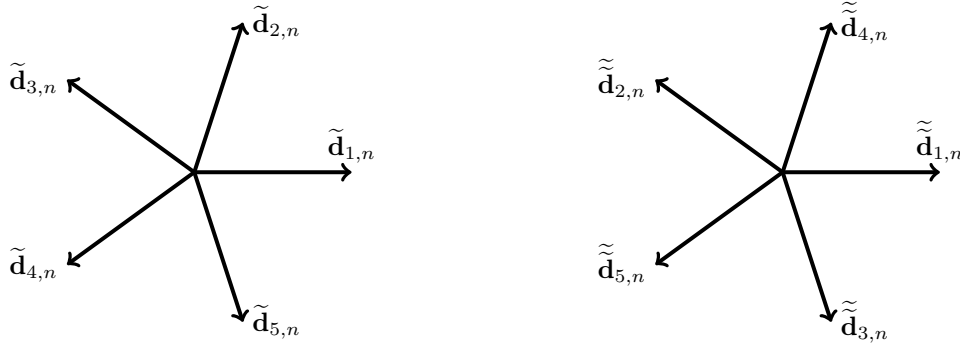


Figure 20: *Left:* equidistributed set of directions $\{\tilde{\mathbf{d}}_{\ell,n}\}_{\ell=1}^{p_{max,n}}$. *Right:* reordered set of directions $\{\tilde{\mathbf{d}}_{\ell,n}\}_{\ell=1}^{p_{max,n}}$. Firstly, one considers the directions with odd index and next those with even index.

point, given the reordered set of directions $\{\tilde{\mathbf{d}}_{\ell,n}\}_{\ell=1}^{p_{max,n}}$, we remove the $2(q_{max,n} - q_K)$ directions having the largest indices. This procedure allows to build elementwise nested sets of directions with different cardinality.

We are now able to define nested spaces over each edge e of the mesh skeleton by fixing spaces of plane waves whose number of basis elements is given by the maximum of the local numbers q_K in (52) of the neighbouring elements:

$$\widetilde{\mathbb{P}\mathbb{W}}_p^c(e) := \begin{cases} \text{span} \left\{ e^{ik\tilde{\mathbf{d}}_{\ell}(\mathbf{x}-\mathbf{x}_e)}|_e : \ell = 1, \dots, 2\max(q_{K_1}, q_{K_2}) + 1 \right\} & \text{if } e \in \mathcal{E}_n^I, e \subseteq \partial K_1 \cap \partial K_2 \\ \text{span} \left\{ e^{ik\tilde{\mathbf{d}}_{\ell}(\mathbf{x}-\mathbf{x}_e)}|_e : \ell = 1, \dots, 2q_K + 1 \right\} & \text{if } e \in \mathcal{E}_n^B, e \subseteq \partial K, \end{cases}$$

where K_1 and K_2 , and K , denote the elements abutting edge e , if e is an interior edge and a boundary edge, respectively. This resembles the so-called *maximum rule* employed in hp -VEM [10].

A sequence of meshes satisfying the geometric refinement condition (51) towards ν , along with the distribution of effective degrees accordingly with (52), is depicted in Figure 21.

In Figure 22, we present the decay of the approximate L^2 errors in (36) in terms of the quadratic root of the number of degrees of freedom. Hereby, we employ the modified version of the method presented in Section 5.1. Further, we select as wave numbers $k = 10, 20$, and 40 , and as grading parameters $\mu = 0.5$ and $\mu = 1/3$, see (51).

We observe a decay of the error which is exponential in terms of the square root of the degrees of freedom instead of the cubic root as for standard hp -FEM [43] and hp -VEM [10]. This is typical of the Trefftz setting, see [30, 32] in the DG framework and [17, 36] in the VEM framework.

Moreover, we want to highlight that after the pre-asymptotic regime, the relative errors decay extremely rapidly in terms of the number of degrees of freedom. This can be explained by the fact that, for smaller mesh sizes, more and more redundant plane wave directions are removed by the

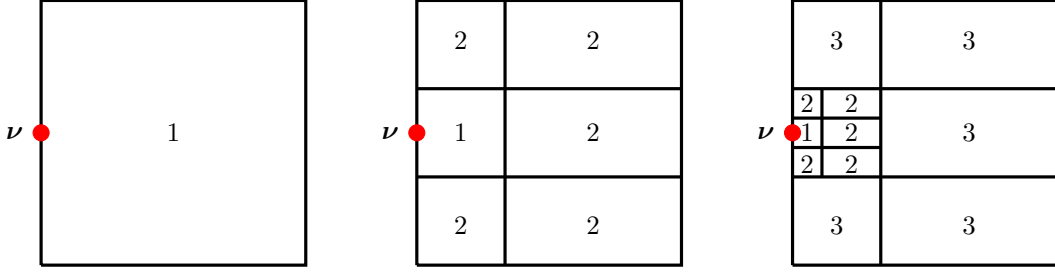


Figure 21: τ_0 (left), τ_1 (center), and τ_2 (right) of a sequence $\{\mathcal{T}_n\}_n$ of meshes graded toward ν with grading parameter $\mu = 1/3$. The numbers inside the elements denote the effective degrees accordingly with (52).

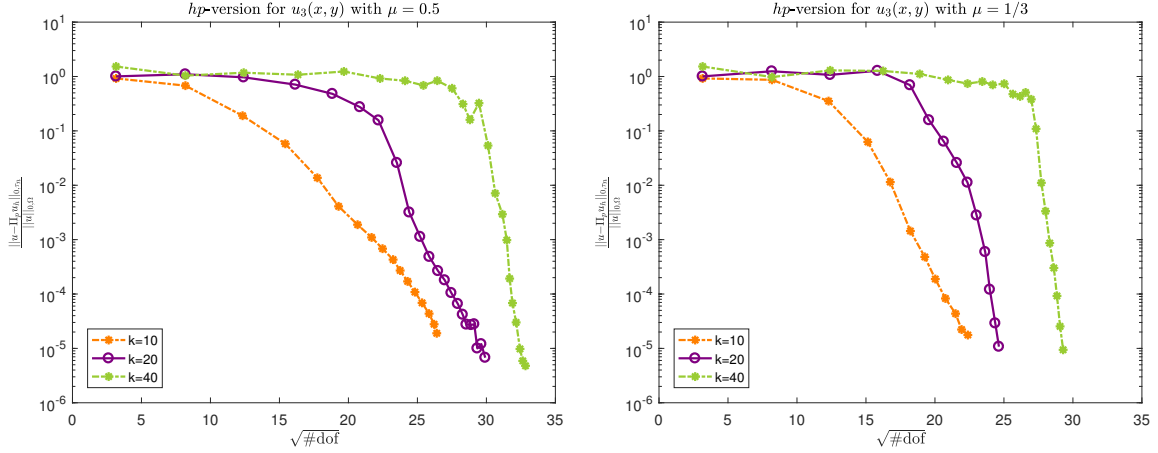


Figure 22: hp -version of the modified method on the test case u_3 in (47), by employing graded meshes as those in Figure 21 with wave numbers $k = 10, 20$, and 40 , and grading parameters $\mu = 0.5$ (left) and $\mu = 1/3$ (right). The distribution of the effective plane wave degree indices is as in (52). In both plots, the approximate L^2 error (36) is plotted against the quadratic root of the number of degrees of freedom.

filtering process, compensating the increase in the number of edges. The “paradox” here is that via the second filtering process in Algorithm 2, the errors of the method decrease exponentially, while the number of degrees of freedom seems to increase extremely slowly, especially in presence of high wave number.

5.3.4 Comparison of the modified nonconforming Trefftz-VEM with the PWVEM

In this section, we compare the approximate relative L^2 errors in (36) of the modified nonconforming Trefftz-VEM with those of the PWVEM [40]. Note that the definition of Π_p^K is the same for both methods. For the PWVEM, we took the stabilization proposed in [40].

We consider a boundary value problem of the form (3) with $\Omega := (0, 1)^2$ and $\Gamma_R = \partial\Omega$, and exact solution u_2 in (47).

h -version: To start with, we compare the h -versions of the methods in terms of the number of degrees of freedom when employing Voronoi meshes. As a first test, we choose $q = 6$ (which corresponds to $p = 13$) and $k = 20, 40$, and 60 . Then, as a second test, we fix instead $k = 20$ and choose $q = 5, 7$, and 9 . The results are shown in Figure 23.

In all the cases, the approximate relative L^2 errors are smaller when using the nonconforming Trefftz-VEM. This can be traced back to the filtering process applied in the Trefftz version.

p -version: For the p -versions, we compare the two methods with $k = 20$ and 40 for the exact solution u_2 in (47) on a Voronoi mesh and a nonconvex polygonal mesh made of 16 and 100 elements, respectively. These meshes are depicted in Figure 24. In Figure 25, the approximate relative L^2 errors are plotted.

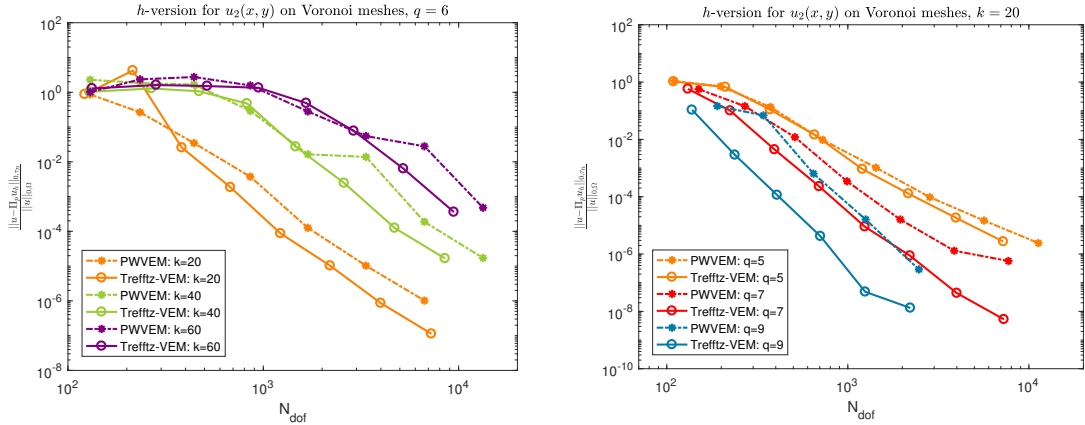


Figure 23: Comparison of the h -version of the modified nonconforming Trefftz-VEM with the PWVEM for u_2 in (47) on Voronoi meshes. *Left:* fixed $q = 6$, different values of $k = 20, 40$, and 60 . *Right:* fixed $k = 20$, different values of $q = 5, 7$, and 9 .

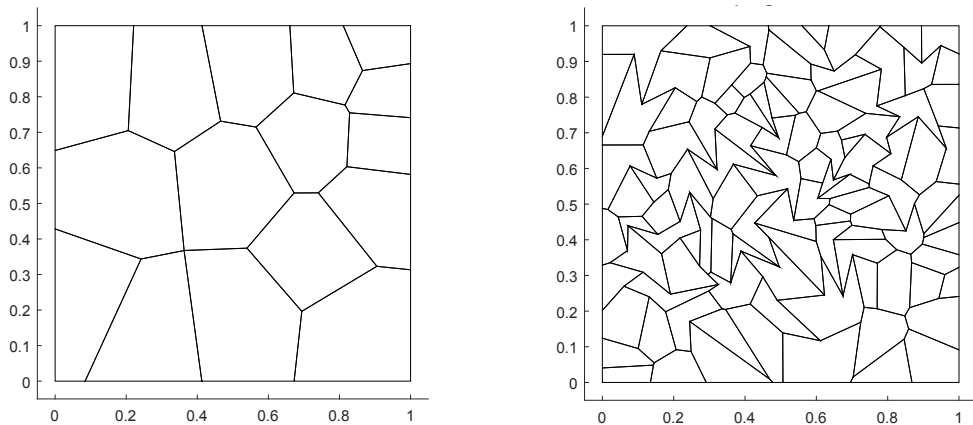


Figure 24: Voronoi mesh with 16 elements (*left*) and a polygonal mesh made of 100 (also nonconvex) elements (*right*).

Also in this case, the modified nonconforming Trefftz-VEM leads to better results, and allows to reach a higher accuracy before instability takes place. In particular, the method seems to be robust even in terms of the geometry of the mesh elements.

Finally, we compare the p -version of the two methods on a structured triangular and a Voronoi mesh with 32 elements each, when using the solution u_3 given in (47), and $k = 10$ and 20 . This is portrayed in Figure 26. In both cases, the convergence rate stagnates after few refinement steps. This is however not surprising, owing to the fact that the solution u_3 in (47) has a low Sobolev regularity.

5.3.5 Comparison of the modified nonconforming Trefftz-VEM with the PWDG

In this section, we compare the approximate relative L^2 errors of the modified nonconforming Trefftz-VEM with those of the PWDG. For the latter, we choose the penalty parameters of the ultra weak formulation in [16]. For all the tests, we employ sequences of Cartesian meshes.

h -version: First, we compare the h -versions of the two methods for a boundary value problem of the form (3) on $\Omega := (0, 1)^2$ with exact solution u_2 given in (47), $\theta = 1$, and $\Gamma_R = \partial\Omega$. The results for fixed $q = 6$ and $k = 20, 40$, and 60 , and fixed $k = 20$ and $q = 5, 7$, and 9 , are reported in Figure 27.

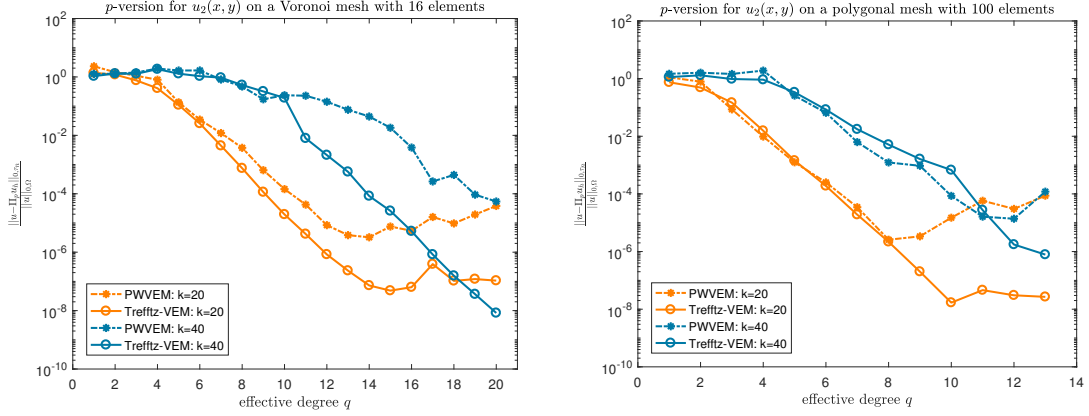


Figure 25: Comparison of the p -version of the modified nonconforming Trefftz-VEM with the PWVEM for u_2 in (47) and $k = 20$ and 40 on the Voronoi mesh with 16 elements (*left*) and the polygonal mesh with 100 (also nonconvex) elements (*right*).

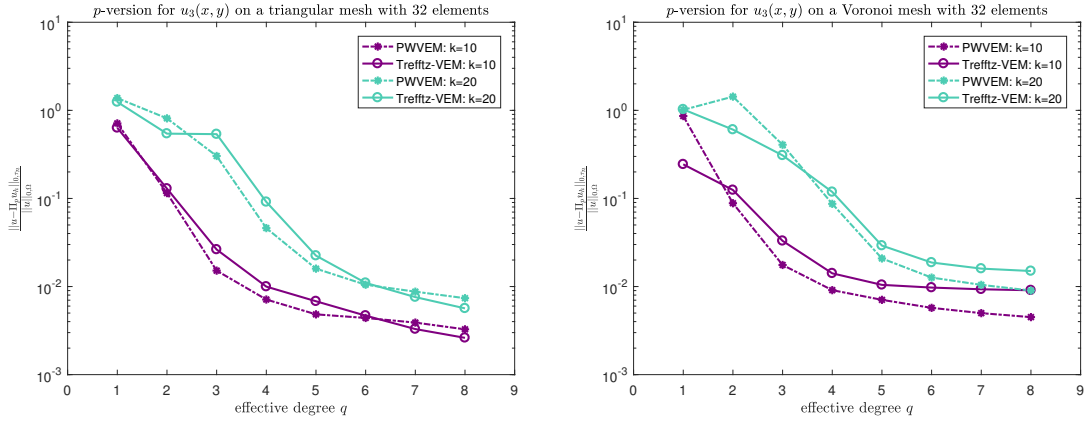


Figure 26: Comparison of the p -version of the modified nonconforming Trefftz VE method with the PWVEM for u_3 in (47), $k = 10$ and 20 , on a triangular mesh and a Voronoi mesh made of 32 elements each.

It can be noticed that, with both methods, we can approximately reach the same accuracy. For the nonconforming Trefftz-VEM, the pre-asymptotic regime is broader, followed however by a “steeper” slope of the convergence rate. This broader pre-asymptotic area can be explained by the fact that, on coarse meshes, the removing procedure of Algorithm 2 is almost not performed, and thus more degrees of freedom than in PWDG are employed, whereas for fine meshes, the removing procedure has a huge impact, see Tables 1 and 2.

Secondly, we perform the same tests as before, considering now as exact solution the function u_3 in (47) instead of u_2 , see Figure 28. We observe a similar behaviour as for the results in Figure 26.

p -version: Concerning the p -version, we compare the approximate relative L^2 bulk errors on a Cartesian mesh made of 16 elements with exact solution given by u_2 in (47) and $k = 20, 40$ and 60 , and exact solution u_3 in (47) and $k = 10$ and 20 , respectively. The numerical results are displayed in Figure 29. Very interestingly, the p -version of the modified nonconforming Trefftz-VEM seems to lead to more robust performance than PWDG, especially for higher wave numbers.

6 Conclusions

In this paper, we extended the nonconforming Trefftz-VEM in [37] to Helmholtz boundary value problems endowed with mixed boundary conditions. We presented a series of numerical exper-

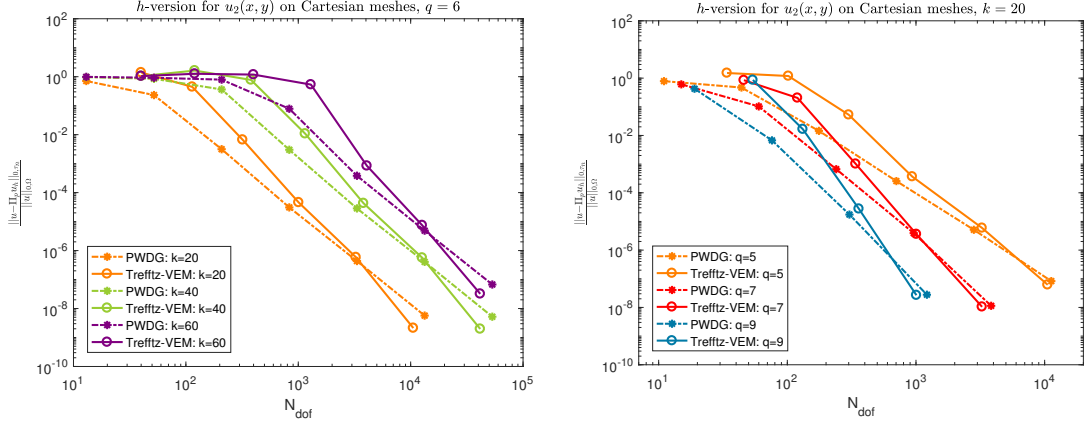


Figure 27: Comparison of the h -version of the modified nonconforming Trefftz-VEM with the PWDG for u_2 in (47) on Cartesian meshes. *Left:* fixed $q = 6$, different values of $k = 20, 40$, and 60 . *Right:* fixed $k = 20$, different values of $q = 5, 7$, and 9 .

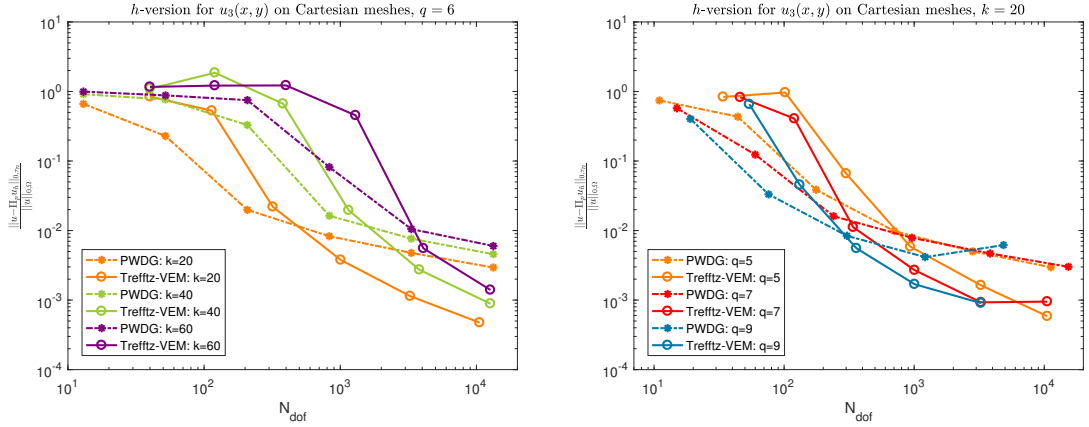


Figure 28: Comparison of the h -version of the modified nonconforming Trefftz VE method with the PWDG for u_3 in (47) on Cartesian meshes. *Left:* fixed $q = 6$, different values of $k = 20, 40$, and 60 . *Right:* fixed $k = 20$, different values of $q = 5, 7$, and 9 .

iments showing that the original version severely suffers of ill-conditioning, making the method practically unreliable.

In order to mitigate the lack of robustness due to the ill-conditioning related to the choice of plane wave basis functions in the design of the method, we built up a numerical recipe based on the orthonormalization of the edge plane wave basis functions via an eigendecomposition of the associated edge mass matrices. We highly exploited the fact that, using the nonconforming setting, it is possible to modify the basis functions edgewise without affecting their behavior on the other edges, which could also be very appealing in regard of an extension of the method to the 3D case and to nonconforming methods for other problems. Using the above-mentioned strategy, the modified nonconforming Trefftz-VEM becomes numerically more stable. Such a recipe also allows for a significant reduction of the number of degrees of freedom.

Numerical experiments confirm the convergence rates derived in [37]. Moreover, the p - and hp -versions of this new method were discussed. We have seen that the modified version of the nonconforming Trefftz-VEM provides in many cases better performance than other plane wave methods for the approximation of solutions to Helmholtz boundary value problems, especially in the case of both high wave numbers and effective degrees.

Extensions of the approach herein presented to the case of piecewise constant wave number are under investigation.

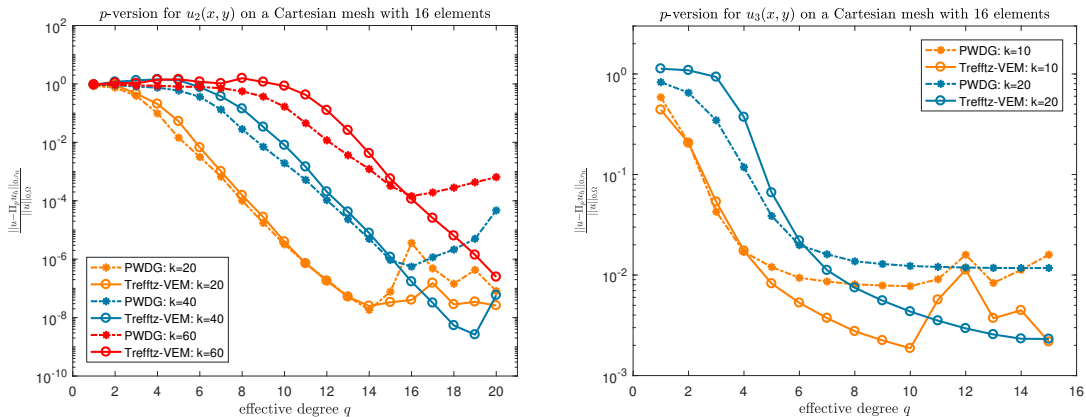


Figure 29: Comparison of the p -version of the modified nonconforming Trefftz-VEM with the PWDG for u_2 in (47), $k = 20, 40$ and 60 (left), and for u_3 in (47), $k = 10$ and 20 (right) on a Cartesian mesh made of 16 elements.

Acknowledgements

The authors have been funded by the Austrian Science Fund (FWF) through the project F 65 (L.M. and I.P.) and the project P 29197-N32 (I.P. and A.P.), and by the Vienna Science and Technology Fund (WWTF) through the project MA14-006 (I.P.).

References

- [1] M. Abramowitz and I. A. Stegun. *Handbook of Mathematical Functions with Formulas, Graphs, and Mathematical Tables*, volume 55. Courier Corporation, 1964.
- [2] P. F. Antonietti, A. Cangiani, J. Collis, Z. Dong, E. H. Georgoulis, S. Giani, and P. Houston. Review of discontinuous Galerkin finite element methods for partial differential equations on complicated domains. In *Building Bridges: Connections and Challenges in Modern Approaches to Numerical Partial Differential Equations*, pages 279–308. Springer, 2016.
- [3] P. F. Antonietti, G. Manzini, and M. Verani. The fully nonconforming virtual element method for biharmonic problems. *Math. Models Methods Appl. Sci.*, 28(02):387–407, 2018.
- [4] N. Aronszajn. A unique continuation theorem for solutions of elliptic partial differential equations or inequalities of second order. *J. Math. Pures Appl.*, 36(9):235–249, 1957.
- [5] B. Ayuso, K. Lipnikov, and G. Manzini. The nonconforming virtual element method. *ESAIM Math. Model. Numer. Anal.*, 50(3):879–904, 2016.
- [6] I. Babuška and J. M. Melenk. The partition of unity finite element method: basic theory and applications. *Comput. Methods Appl. Mech. Engrg.*, 139(1-4):289–314, 1996.
- [7] L. Beirão da Veiga, F. Brezzi, A. Cangiani, G. Manzini, L.D. Marini, and A. Russo. Basic principles of virtual element methods. *Math. Models Methods Appl. Sci.*, 23(01):199–214, 2013.
- [8] L. Beirão da Veiga, F. Brezzi, L.D. Marini, and A. Russo. The hitchhiker’s guide to the virtual element method. *Math. Models Methods Appl. Sci.*, 24(8):1541–1573, 2014.
- [9] L. Beirão da Veiga, A. Chernov, L. Mascotto, and A. Russo. Basic principles of hp virtual elements on quasiuniform meshes. *Math. Models Methods Appl. Sci.*, 26(8):1567–1598, 2016.
- [10] L. Beirão da Veiga, A. Chernov, L. Mascotto, and A. Russo. Exponential convergence of the hp virtual element method with corner singularity. *Numer. Math.*, 138(3):581–613, 2018.
- [11] L. Beirão da Veiga, F. Dassi, and A. Russo. High-order virtual element method on polyhedral meshes. *Comput. Math. Appl.*, 74:1110–1122, 2017.
- [12] L. Beirão da Veiga, K. Lipnikov, and G. Manzini. *The Mimetic Finite Difference Method for elliptic problems*, volume 11. Springer, 2014.
- [13] A. Cangiani, V. Gyrya, and G. Manzini. The non-conforming virtual element method for the Stokes equations. *SIAM J. Numer. Anal.*, 54(6):3411–3435, 2016.
- [14] A. Cangiani, G. Manzini, and O. J. Sutton. Conforming and nonconforming virtual element methods for elliptic problems. *IMA J. Numer. Anal.*, 37:1317–1354, 2016.
- [15] S. Cao and L. Chen. Anisotropic error estimates of the linear nonconforming virtual element methods. <https://arxiv.org/abs/1806.09054>, 2018.

- [16] O. Cessenat and B. Després. Application of an ultra weak variational formulation of elliptic PDEs to the two-dimensional Helmholtz problem. *SIAM J. Numer. Anal.*, 35(1):255–299, 1998.
- [17] A. Chernov and L. Mascotto. The harmonic virtual element method: stabilization and exponential convergence for the Laplace problem on polygonal domains, 2018. doi: <https://doi.org/10.1093/imanum/dry038>.
- [18] B. Cockburn, J. Gopalakrishnan, and R. Lazarov. Unified hybridization of discontinuous Galerkin, mixed, and continuous Galerkin methods for second order elliptic problems. *SIAM J. Numer. Anal.*, 47(2):1319–1365, 2009.
- [19] D. Colton and R. Kress. *Inverse Acoustic and Electromagnetic Scattering Theory*, volume 93. Springer, Heidelberg, 2nd edition, 1998.
- [20] M. Crouzeix and P.-A. Raviart. Conforming and nonconforming finite element methods for solving the stationary Stokes equations. *RAIRO Anal. Numér.*, 7(R3):33–75, 1973.
- [21] F. Dassi and L. Mascotto. Exploring high-order three dimensional virtual elements: bases and stabilizations. *Comput. Math. Appl.*, 75(9):3379–3401, 2018.
- [22] E. Deckers, O. Atak, L. Coox, R. D’Amico, H. Devriendt, S. Jonckheere, K. Koo, B. Pluymers, D. Vandepitte, and W. Desmet. The wave based method: An overview of 15 years of research. *Wave Motion*, 51(4):550–565, 2014.
- [23] D. A. Di Pietro and A. Ern. Hybrid high-order methods for variable-diffusion problems on general meshes. *C. R. Math. Acad. Sci. Paris*, 353(1):31–34, 2015.
- [24] C. Farhat, I. Harari, and L. P. Franca. The discontinuous enrichment method. *Comput. Methods Appl. Mech. Engrg.*, 190(48):6455–6479, 2001.
- [25] F. Gardini, G. Manzini, and G. Vacca. The nonconforming virtual element method for eigenvalue problems. <http://arxiv.org/abs/1802.02942>, 2018.
- [26] C. J. Gittelsohn. Plane wave discontinuous Galerkin methods. Master’s thesis, SAM-ETH Zürich, 2008.
- [27] C. J. Gittelsohn, R. Hiptmair, and I. Perugia. Plane wave discontinuous Galerkin methods: analysis of the h -version. *ESAIM Math. Model. Numer. Anal.*, 43(2):297–331, 2009.
- [28] I.G. Graham and S.A. Sauter. Stability and error analysis for the Helmholtz equation with variable coefficients. <https://arxiv.org/abs/1803.00966>, 2018.
- [29] R. Hiptmair, A. Moiola, and I. Perugia. Plane wave discontinuous Galerkin methods for the 2D Helmholtz equation: analysis of the p -version. *SIAM J. Numer. Anal.*, 49(1):264–284, 2011.
- [30] R. Hiptmair, A. Moiola, and I. Perugia. Plane wave-discontinuous Galerkin methods: exponential convergence of the hp -version. *Found. Comput. Math.*, 16(3):637–675, 2016.
- [31] R. Hiptmair, A. Moiola, and I. Perugia. A survey of Trefftz methods for the Helmholtz equation. In *Building bridges: connections and challenges in modern approaches to numerical partial differential equations*, pages 237–279. Springer, 2016.
- [32] R. Hiptmair, A. Moiola, I. Perugia, and C. Schwab. Approximation by harmonic polynomials in star-shaped domains and exponential convergence of Trefftz hp -dGFEM. *ESAIM Math. Model. Numer. Anal.*, 48(3):727–752, 2014.
- [33] K. Lipnikov, G. Manzini, and M. Shashkov. Mimetic finite difference method. *J. Comput. Phys.*, 257:1163–1227, 2014.
- [34] X. Liu and Z. Chen. The nonconforming virtual element method for the Navier-Stokes equations. *Adv. Comput. Math.*, 2018. doi: <https://doi.org/10.1007/s10444-018-9602-z>.
- [35] L. Mascotto. Ill-conditioning in the virtual element method: Stabilizations and bases. *Numer. Methods Partial Differential Equations*, 34(4):1258–1281, 2018.
- [36] L. Mascotto, I. Perugia, and A. Pichler. Non-conforming harmonic virtual element method: h - and p -versions. <https://arxiv.org/abs/1801.00578>, 2018.
- [37] L. Mascotto, I. Perugia, and A. Pichler. A nonconforming Trefftz virtual element method for the Helmholtz problem. <https://arxiv.org/abs/1805.05634>, 2018.
- [38] W. C. H. McLean. *Strongly Elliptic Systems and Boundary Integral Equations*. Cambridge University Press, 2000.
- [39] P. Monk and D.-Q. Wang. A least-squares method for the Helmholtz equation. *Comput. Methods Appl. Mech. Engrg.*, 175(1-2):121–136, 1999.
- [40] I. Perugia, P. Pietra, and A. Russo. A plane wave virtual element method for the Helmholtz problem. *ESAIM Math. Model. Numer. Anal.*, 50(3):783–808, 2016.
- [41] H. Riou, P. Ladeveze, and B. Sourcis. The multiscale VTCR approach applied to acoustics problems. *J. Comput. Acoust.*, 16(04):487–505, 2008.
- [42] S. Rjasanow and S. Weißer. Higher order BEM-based FEM on polygonal meshes. *SIAM J. Numer. Anal.*, 50(5):2357–2378, 2012.
- [43] C. Schwab. *p - and hp - Finite Element Methods: Theory and Applications in Solid and Fluid Mechanics*. Clarendon Press Oxford, 1998.
- [44] C. Talischi, G. H. Paulino, A. Pereira, and I. F. M. Menezes. PolyMesher: a general-purpose mesh generator for polygonal elements written in Matlab. *Struct. Multidiscip. Optim.*, 45:309–328, 2012.
- [45] H. Triebel. *Interpolation theory, function spaces, differential operators*. North-Holland, 1978.
- [46] J. Zhao, S. Chen, and B. Zhang. The nonconforming virtual element method for plate bending problems. *Math. Models Methods Appl. Sci.*, 26(09):1671–1687, 2016.